Inorganic Chemistry

Article

pubs.acs.org/IC

Broken Symmetry DFT Calculations/Analysis for Oxidized and Reduced Dinuclear Center in Cytochrome *c* Oxidase: Relating Structures, Protonation States, Energies, and Mössbauer Properties in *ba*$_3$ *Thermus thermophilus*

Wen-Ge Han Du and Louis Noodleman*

Department of Integrative Structural and Computational Biology, CB213, The Scripps Research Institute, 10550 North Torrey Pines Road, La Jolla, California 92037, United States

Supporting Information

ABSTRACT: The $Fe_{a3}^{3+}\cdots Cu_B^{2+}$ dinuclear center (DNC) structure of the as-isolated oxidized *ba*$_3$ cytochrome *c* oxidase (C*c*O) from *Thermus thermophilus* (*Tt*) is still not fully understood. When the proteins are initially crystallized in the oxidized state, they typically become radiolyticly reduced through X-ray irradiation. Several X-ray crystal structures of reduced *ba*$_3$ C*c*O from *Tt* are available. However, depending on whether the crystals were prepared in a lipidic cubic phase environment or in detergent micelles, and whether the C*c*O's were chemically or radiolyticly reduced, the X-ray diffraction analysis of the crystals showed different $Fe_{a3}^{2+}\cdots Cu_B^{+}$ DNC structures. On the other hand, Mössbauer spectroscopic experiments on reduced and oxidized *ba*$_3$ C*c*Os from *Tt* (Zimmermann et al., *Proc. Natl. Acad. Sci. USA* 1988, 85, 5779−5783) revealed multiple $^{57}Fe_{a3}^{2+}$ and $^{57}Fe_{a3}^{3+}$ components. Moreover, one of the $^{57}Fe_{a3}^{3+}$ components observed at 4.2 K transformed from a proposed "low-spin" state to a different high-spin species when the temperature was increased above 190 K, whereas the other high-spin $^{57}Fe_{a3}^{3+}$ component remained unchanged. In the current Article, in order to understand the heterogeneities of the DNC in both Mössbauer spectra and X-ray crystal structures, the spin crossover of one of the $^{57}Fe_{a3}^{3+}$ components, and how the coordination and spin states of the $Fe_{a3}^{3+/2+}$ and $Cu^{2+/1+}$ sites relate to the heterogeneity of the DNC structures, we have applied density functional OLYP calculations to the DNC clusters established based on the different X-ray crystal structures of *ba*$_3$ C*c*O from *Tt*. As a result, specific oxidized and reduced DNC structures related to the observed Mössbauer spectra and to spectral changes with temperature have been proposed. Our calculations also show that, in certain intermediate states, the His233 and His283 ligand side chains may dissociate from the Cu_B^{+} site, and they may become potential proton loading sites during the catalytic cycle.

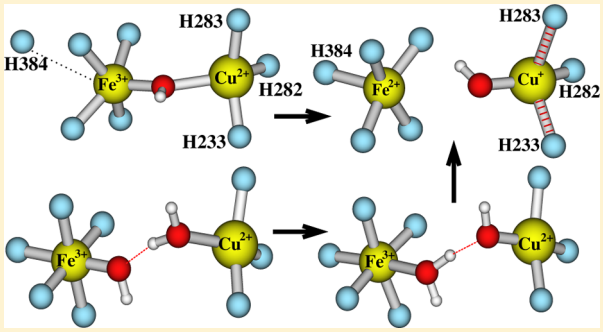

1. INTRODUCTION

Located in the inner mitochondrial membrane in eukaryotes or alternatively in the periplasmic membrane in aerobic bacteria, cytochrome *c* oxidase (C*c*O) is the terminal enzyme in the respiratory chain that reduces O_2 to H_2O and pumps protons across the membrane.[1−4] The catalytic site of C*c*O, which binds and reduces O_2, contains a heme A (Fe_{a3}) and a Cu ion (Cu_B), forming the dinuclear (or binuclear) center (DNC or BNC). Cu_B is in the proximity (∼5 Å) of Fe_{a3}.[5−15] In addition, C*c*O protein contains another two redox centers: a homodinuclear Cu dimer (Cu_A), which serves as the initial site of electron entry to C*c*O,[16,17] and another heme, which is heme A (Fe_a) in the case of the *aa*$_3$ type of C*c*O or heme B (Fe_b) in the *ba*$_3$ type.

Zimmermann et al. reported Mössbauer spectra of the as-isolated oxidized and reduced *ba*$_3$ C*c*O from *Thermus thermophilus* (*Tt*).[18] In the reduced state, two high-spin ferrous components (at 4.2 K) were observed for the Fe_{a3} site with the majority component (86%) having an isomer shift δ = 0.95 mm s^{-1} and quadrupole splitting ΔE_Q = 1.43 mm s^{-1} and a minority species (14%) with δ = 0.92 mm s^{-1} and ΔE_Q = 2.34 mm s^{-1}.[18] The oxidized state was even more complicated. When the temperature was between 4.2 and 190 K, the Mössbauer spectra revealed two components attributable to $^{57}Fe_{a3}^{3+}$: a quadrupole doublet with splitting ΔE_Q = 0.71 mm s^{-1} and δ = 0.41 mm s^{-1}, which was proposed to be a high-spin (HS) ferric heme and accounts for ∼46% of $^{57}Fe_{a3}^{3+}$, and a second doublet (54%) with ΔE_Q = 2.24 mm s^{-1} and δ = 0.29 mm s^{-1}, which was proposed to be a low-spin (LS) ferric heme.[18] When the temperature was >190 K, the "low-spin" $^{57}Fe_{a3}^{3+}$ component was reported to undergo a transition to "high-spin" that was essentially complete at 245 K. However, the new "high-spin" compound yielded $\Delta E_Q \approx$ 1 mm s^{-1}, and the two distinct "high-spin" species (ΔE_Q = 0.7 and ∼1 mm s^{-1}) coexisted at

Received: March 27, 2015
Published: July 20, 2015

DOI: 10.1021/acs.inorgchem.5b00700
Inorg. Chem. 2015, 54, 7272−7290

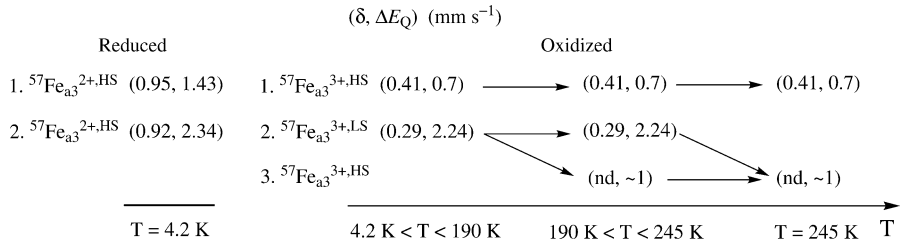

Figure 1. Data summarized from ref 18. The observed $^{57}Fe_{a3}{}^{2+}$ and $^{57}Fe_{a3}{}^{3+}$ Mössbauer isomer shifts (δ, mm s^{-1}) and quadrupole splittings (ΔE_Q, mm s^{-1}) for ba_3 C*c*O from *Tt* and the spectra variation with temperature (T).[18] Note that only $\Delta E_Q \approx 1$ mm s^{-1} was given in ref 18. for the third $^{57}Fe_{a3}{}^{3+}$ species (HS state), which was transformed from the second $^{57}Fe_{a3}{}^{3+}$ species (supposed to be in LS state) as the temperature increased to >190 K, and the transition was complete at 245 K. "nd" stands for "not determined from experiment".

Table 1. Resolutions (Å) and the Main DNC Geometrical Parameters (Å) of the Reduced X-ray Crystal Structures of ba_3 C*c*O from *Tt* and the Experimental $^{57}Fe_{a3}{}^{2+}$ Mössbauer Isomer Shifts (δ, mm s^{-1}) and Quadrupole Splittings (ΔE_Q, mm s^{-1}) for the Reduced DNC in Different Cytochrome Oxidase Proteins

crystal structure	resolution	Fe−N (H384)	Fe−O/Fe−O1	O1−O2	Cu−O/Cu−O2	Fe···Cu	Cu−N (H233)	Cu−N (H282)	Cu−N (H283)	O···O (Y237)	ref
1EHK	2.4	3.31	2.26		2.31	4.40	2.10	2.22	2.13	2.52	10
1XME	2.3	2.48	2.44		2.07	4.39	1.96	1.96	1.97	2.67	11
3EH4	2.9	2.39	3.08		2.20	4.73	1.96	2.03	1.97	2.47	12
3EH3	3.1	2.39				5.06	1.92	2.05	2.06	2.91	12
3EH5	2.8	2.10				5.04	2.16	1.94	2.18	2.61	12
3S8F	1.8	2.09	2.25	1.54	2.29	4.87	1.94	1.99	1.91	2.56	15
3S8G	1.8	2.22	2.39	1.52	2.25	4.92	1.95	2.03	1.98	2.66	15

cytochrome oxidase		δ	ΔE_Q	ref
ba_3 from *T. thermophilus*	1st:	0.95	1.43	18
	2nd:	0.92	2.34	18
c_1aa_3 from *T. thermophilus*		0.96 ± 0.03	2.06 ± 0.05	54
aa_3 from bovine heart		0.93 ± 0.06	1.85 ± 0.10	55

245 K.[18] For easier comparison, we assembled the $^{57}Fe_{a3}{}^{3+/2+}$ Mössbauer experimental data of ba_3 C*c*O from *Tt* in Figure 1.

Currently, detailed DNC structures and comparative energies in the as-isolated, fully oxidized, and fully reduced states of C*c*O are still not clear.[1−3,6,7,10−15,19−22] Although crystals of the fully oxidized as-isolated C*c*Os were well prepared, when exposed to X-ray irradiation, the metal sites are easily reduced.[12,13,15] Several reduced X-ray crystal structures of ba_3 C*c*O from *Tt* have been obtained.[10−12,15] However, depending on whether the crystals were prepared in a lipidic cubic phase environment or in detergent micelles, and whether the C*c*Os were chemically or radiolyticly reduced, X-ray diffraction analyses of the crystals obtained from different protocols show different DNC structures.[12,15] The PDB entries of these *Tt* X-ray structures are 1EHK,[10] 1XME,[11] 3EH3,[12] 3EH4,[12] 3EH5,[12] 3S8F,[15] and 3S8G,[15] in which both 3S8F (wild-type) and 3S8G (A120F mutant) were obtained in a lipidic cubic phase environment and others in detergent micelles. 1EHK, 1XME, 3EH4, 3S8F, and 3S8G are radiation-reduced crystal structures. 3EH3 and 3EH5 represent chemically reduced X-ray crystal structures. However, 3EH3 was obtained by chemically reducing the crystals of the oxidized, as-isolated protein, and 3EH5 was obtained by a path in which the oxidized as-isolated proteins were reduced with dithionite in an anaerobic environment prior to being crystallized and frozen in liquid nitrogen.[12]

The resolutions and the main geometric parameters in the DNCs from these X-ray structures are compared in Table 1. As an example, the DNC of 1EHK is shown in Figure 2. In the observed structures, the Fe_{a3} site has one axial histidine ligand (His384), and the Cu_B site has three histidine ligands: His233, His282, and His283. His233 covalently links with Tyr237, a

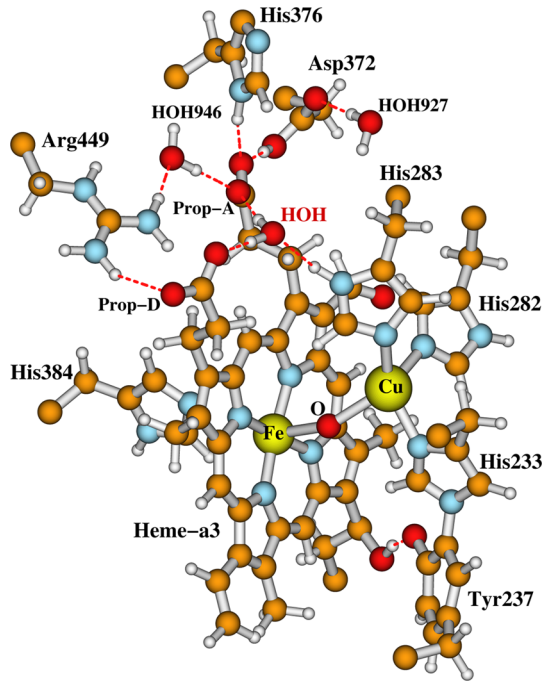

Figure 2. Fe−Cu DNC of the X-ray radiolyticly reduced crystal structure 1EHK (2.4 Å resolution),[10] which was obtained for the native *Tt* ba_3 C*c*O solubilized in detergent micelles. The protonation state of the Tyr237 side chain and the oxygen species between the Fe and Cu sites in the DNC are not known from the X-ray crystal structure alone. A water molecule ("HOH" in red) was added based on other X-ray structures.

DOI: 10.1021/acs.inorgchem.5b00700
Inorg. Chem. 2015, 54, 7272−7290

linkage that is common to all C*c*Os but is otherwise unknown in metalloenzymes. These structures obviously vary in the $Fe_{a3}\cdots Cu_B$ distances, in what resides in the space between the Fe_{a3} and Cu_B sites, and in the Fe_{a3}–ligand distances. Because only the DNC of C*c*O is studied in the current Article, for simplicity, the Fe_{a3} and Cu_B will be noted as Fe and Cu hereafter. An open $Fe^{2+}\cdots Cu^{+}$ (with no atoms between Fe^{2+} and Cu^{+}) DNC structure was obtained in 3EH3 and 3EH5.[12] A bridging oxygen species was observed between the Fe^{2+} and Cu^{+} sites in 1EHK (Figure 2),[10] where the His384 side chain was found to be far from the Fe atom with an Fe···N(His384) distance of 3.31 Å. In 1XME[11] and 3EH4,[12] an oxygen species is also found in the space between Fe^{2+} and Cu^{+}, but it appears bound only to the Cu^{+} site, and the axial His384 side chain ligand is much closer to the Fe^{2+} site. Although the bound solvent was called "the water molecule residing between Fe and Cu" in later publications,[12] it is not evident whether this oxygen species in the DNC's of 1EHK, 1XME, and 3EH4 is a water molecule (H_2O) or a hydroxide anion (OH^-).[10]

Further, a peroxide-type dioxygen species bridging the $Fe^{2+}\cdots Cu^{+}$ DNC was observed in both 3S8F and 3S8G.[15] To evaluate whether this bridging dioxygen species is O_2^{2-}, $O_2^{\cdot-}$, HO_2^-, or H_2O_2, in ref 23 we performed a series of density functional theory (DFT) calculations (using the OLYP[24,25] functional) on the quantum cluster models based on 3S8G DNC and have proposed that the X-ray crystal structure 3S8G is likely to represent the superposition of the Fe^{2+}-(HO_2^-)-Cu^{+} DNC's in different states (Fe^{2+} in low-spin, intermediate-spin, or high-spin) with the majority species having the proton of the HO_2^- residing on the oxygen atom that is closer to the Fe^{2+} site in the Fe^{2+}-(HO-O)$^-$-Cu^{+} conformation.[23]

Clearly, the X-ray crystal structures and the Mössbauer experiments show structural heterogeneity within the DNC of ba_3 C*c*O from *Tt*. Relating the detailed structures of the oxidized and reduced DNC's is an essential step in analyzing the path(s) by which C*c*O reduces O_2 to H_2O and in finding what paths effectively couple O_2 reduction chemistry to proton pumping across the membrane. In the current Article, we continue our DFT calculations on DNC models starting from different X-ray crystal structures to address the following questions: (1) Is the bridging/Cu-binding oxygen species observed in the DNC's of 1EHK, 1XME, and 3EH4 an H_2O molecule or an OH^- anion? (2) How do the axial His384 and nearby solvent ligands influence the $^{57}Fe^{2+}$ Mössbauer properties? (3) What are the DNC structures representing the two $^{57}Fe_{a3}{}^{2+}$ components observed in Mössbauer experiments, and what do the DFT calculations predict for Fe^{2+} spin states and their relative energies in the DNC? (4) Will the geometry optimized 3S8G-Fe^{2+}-(HO_2^-)-Cu^{+} DNC structures obtained in ref 23 reproduce the Mössbauer properties of any of the two $^{57}Fe_{a3}{}^{2+}$ components? (5) What are the feasible DNC structures of the three $^{57}Fe_{a3}{}^{3+}$ components observed in the Mössbauer experiments? (6) How does spin-crossover link different states and structures in the transition of Fe^{3+}(state 2) → Fe^{3+}(state 3) when the temperature is increased from 190 to 245 K (Figure 1)? (7) What do the comparative structures and energies tell us about potential reaction pathways and protonation states (especially for Tyr237) in this early part of the catalytic cycle?

2. MODELS AND CALCULATIONAL METHODS

Several water molecules are normally found above the DNC that have H-bonding interactions with the two propionate carboxylate groups (prop-A and prop-D) and the side chains of Arg449 and Asp372. In many C*c*O X-ray crystal structures,[6,11−15] a water molecule ("HOH" in red) was observed in a position to have hydrogen bonding interactions with both prop-A and prop-D and also with the His283 side chain (Figure 2). However, this water molecule was not present in the 1EHK.pdb file. We are not sure if this water molecule missed detection in 1EHK or if it is displaced (a water molecule HOH941 above this position was observed in 1EHK). To be consistent with the calculations for the DNC clusters of other X-ray crystal structures, we also placed a water molecule in this position (HOH) for the 1EHK DNC calculations.

The O···O distance between the carboxylate groups of Prop-A and Asp372 side chain in 1EHK is only 2.49 Å. Therefore, the Asp372 side chain is likely in the neutral protonated state and has a H-bonding interaction with the anionic carboxylate group of prop-A.[17] Prop-A also H-bonds to $HN_{\delta 1}$ of His376 side chain with an $O\cdots N_{\delta 1}$ distance of 2.90 Å. $N_{\varepsilon 2}$ (near the top of Figure 2) of the His376 side chain is within a strong H-bonding distance (2.68 Å) with one of the oxygen atoms of the carboxylate group of Glu126B side chain (not shown in Figure 2). Therefore, the His376 side chain is likely in the neutral state, and its $N_{\varepsilon 2}$ site H-bonds to the neutral protonated Glu126B side chain.

The initial geometries of our DNC models are taken from the different X-ray crystal structures. The size of the model clusters taken from 1EHK, 3EH3, 3EH4, and 3EH5 is the same as shown in Figure 2 (but with different species between the Fe and Cu sites). No water molecules were reported in 3EH3.pdb, we therefore manually added the three water molecules above the DNC in that structure according to their relative positions in 3EH5.pdb. The ending $C_\alpha/C_\gamma/C_{\text{geranyl-side chain}}$ atoms shown in Figure 2 were each replaced by a link hydrogen (H_{link}) atom along the original C−C direction with the C−H_{link} distance of 1.09 Å. The positions of the H_{link} atoms that replace the C_α/C_γ atoms were fixed during all geometry optimization calculations.

Additional crystallographic water molecules near the DNC were observed in 3S8G and 3S8F compared to the other structures. The size of the model cluster taken from 3S8G, which was used in both ref 23 and in the current study is a little larger than that in Figure 2 by including the Gly232 residue and four more water molecules that are in the positions of HOH604, HOH608, HOH607, and HOH610 in 3S8G (see Figures 1 and 2 of ref 23).

On the basis of the calculations for relative spin-state energetics of Fe^{2+} and Fe^{3+} heme models performed by Vancoillie et al.,[26] none of the tested density functionals (B3LYP, B3LYP*, OLYP, BP86, TPSS, TPSSh, M06, or M06-L) consistently provide better accuracy than CASPT2 (multi-configurational perturbation theory) for all their model complexes against available high-level coupled cluster singles and doubles (CCSD) results. However, the pure functional OLYP yields similar results to the hybrid functionals B3LYP* and B3LYP. And for their large heme models, the results of OLYP, B3LYP, and B3LYP* are reasonably close to the best estimate of the spin-splittings with errors typically ≤6 kcal mol^{-1}.[26] Radoń and Pierloot also investigated the performance of the CASSCF/CASPT2 approach and several DFT functionals (PBE0, B3LYP, BP86, and OLYP) in calculating the bonding of CO, NO, and O_2 molecules to two model heme systems.[27] They found that the experimentally available binding energies are best reproduced by the CASPT2 method and with the OLYP functional. The CASSCF spin populations most

DOI: 10.1021/acs.inorgchem.5b00700
Inorg. Chem. 2015, 54, 7272−7290

closely correspond to the results obtained with the pure OLYP or BP86 rather than with the hybrid functionals.[27] Therefore, we used the OLYP functional in studying the 3S8G-DNC[23] geometric and energetic properties and will continue using this functional in the current study.

The DNC model geometries were optimized using the Amsterdam Density Functional Package (ADF2012.01)[28−30] with integration grid accuracy parameter 4.0 within the conductor-like screening (COSMO) solvation model.[31−34] Because both the cluster and the surrounding protein environment are quite polar and contain many water molecules, to be consistent with refs 17 and 23, a large dielectric constant of a simple ketone (ε = 18.5) was applied to the environment in all COSMO calculations. The van der Waals radii of 1.5, 1.4, 1.7, 1.52, 1.55, and 1.2 Å were used for atoms Fe, Cu, C, O, N, and H, respectively.[17,23] During geometry optimizations, the all-electron triple-ζ plus polarization (TZP) Slater-type basis set was applied for the major atoms at the DNC, including $Fe^{3+/2+}$, $Cu^{2+/1+}$, the oxygen species (H_2O or OH^-) between $Fe^{3+/2+}$ and $Cu^{2+/1+}$, and all the N atoms binding with $Fe^{3+/2+}$/$Cu^{2+/1+}$, and the double-ζ plus polarization (DZP) basis set with frozen cores of C(1s), N(1s), and O(1s) was applied to the rest of the atoms.

The Fe^{2+} and Fe^{3+} sites may exist in one of the three spin states: low-spin (LS) with S_{Fe2+} = 0 and S_{Fe3+} = 1/2, intermediate-spin (IS) with S_{Fe2+} = 1 and S_{Fe3+} = 3/2, or high-spin (HS) with S_{Fe2+} = 2 and S_{Fe} = 5/2. The Cu^+ has spin S_{Cu+} = 0, and Cu^{2+} has S_{Cu2+} = 1/2. Further, the Fe^{3+} site may couple with the Cu^{2+} site ferromagnetically (F) with a total spin $S_{total} = S_{Fe3+} + S_{Cu2+}$ or antiferromagnetically (AF) with $S_{total} = S_{Fe3+} - S_{Cu2+}$. The AF-coupling spin state cannot be obtained directly from the normal DFT calculations. As in previous work,[23,35−42] we represent the AF spin-coupled state in DFT by a "broken-symmetry" (BS) state,[43−45] where a spin-unrestricted determinant is constructed in which the Fe^{3+} site has spin-up electrons as majority spin and the Cu^{2+} site has majority spin-down electrons.

After geometry optimizations, to obtain more accurate energies (which will be reported in the Results section) and the Mössbauer isomer shift and quadrupole splitting properties, we applied a single-point energy calculation at each optimized geometry using an all-electron/all-TZP basis set to all atoms within the COSMO solvation model. Our own program is then used to calculate the electron density $\rho(0)$ at the Fe nuclei.[40,46,47] The Mössbauer isomer shift δ is calculated based on $\rho(0)$

$$\delta = \alpha[\rho(0) - A] + C \tag{1}$$

A is a constant and taken as 11877. In our previous study,[40] α = −0.328, C = 0.622 mm s^{-1} for $^{57}Fe^{2+}$ and α = −0.307, C = 0.385 mm s^{-1} for $^{57}Fe^{3+}$ were obtained from linear regression between the measured isomer shifts and OLYP-calculated electron densities at Fe nuclei of 17 $Fe^{2+,2.5+}$ complexes (31 total Fe sites) and 19 $Fe^{2.5+,3+,3.5+,4+}$ complexes (30 total Fe sites), respectively.

The electric field gradient (EFG) at the Fe nucleus obtained from the all-electron/all-TZP single-point energy calculation is used to calculate the Mössbauer quadrupole splitting (ΔE_Q) property. Normally, the EFG tensors V are diagonalized and the eigenvalues are reordered such that $|V_{zz}| \geq |V_{yy}| \geq |V_{xx}|$. The asymmetry parameter η is defined as

$$\eta = (V_{xx} - V_{yy})/V_{zz} \tag{2}$$

Then, the ΔE_Q for ^{57}Fe of the nuclear excited state (I = 3/2) can be calculated as

$$\Delta E_Q = (1/2)eQV_{zz}(1 + \eta^2/3)^{1/2} \tag{3}$$

where e is the electrical charge of a positive electron, and Q is the nuclear quadrupole moment of Fe. Recently, the ADF software package determines the ΔE_Q value using eQ = 0.16 electron-barn.[48] We will report the ADF-calculated ΔE_Q values in the current study.

A few comments outlining how different state energies are compared should prove helpful. Using the ADF code, state energies are defined with respect to a sum of reference fragment energies (reference atoms in the present case). Then, these electronic energies E can be directly compared when the states have the same atom compositions (types and numbers of atoms). Such states are isomers (tautomers). When there are proton transfers between tautomers, ΔE can be defined by adding the ΔZPE difference between states (see below). Further, when considering net deprotonation/protonation, the H^+ reference energy in the gas phase and in aqueous solution must be included, as discussed next. Systems differing in the total number of water molecules cannot be directly compared in energies because an H_2O (in bulk aqueous solvent) reference energy is also needed. This H_2O gas phase and H_2O in solvent energy reference was presented in our earlier works (refs 17 and 42) but is not a focus in this paper.

To determine the protonation state of the oxygen species residing between the Fe and Cu sites and of the Tyr237 side chain, we performed pK_a calculations for certain states using[23,42]

$$1.37\mathrm{p}K_a = E(A^-) - E(AH) + E(H^+) + \Delta G_{sol}(H^+, 1\ \mathrm{atm}) - T\Delta S_{gas}(H^+) + \Delta ZPE + (5/2)RT \tag{4}$$

where $E(A^-)$ and $E(AH)$ are the calculated energies of the deprotonated and protonated states, $\Delta G_{sol}(H^+,1\ \mathrm{atm})$ is the solvation free energy of a proton at 1 atm pressure. We use the "best available" experimental value of −264.0 kcal mol^{-1} for this term based on analysis of cluster-ion solvation data.[49−51] Unlike in ref 23, where $E(H^+)$ was calculated as the energy of a proton (in gas-phase with OLYP potential) with respect to a spin-restricted hydrogen atom, here, we take the empirically corrected $E(H^+)$ = 12.71 eV = 293.1 kcal mol^{-1} based on experimental standard hydrogen electrode energy and the proton solvation free energy (see appendix in ref 42). The translational entropy contribution to the gas-phase free energy of a proton is taken as $-T\Delta S_{gas}(H^+)$ = −7.8 kcal mol^{-1} at 298 K and 1 atm pressure.[52] $(5/2)RT$ = 1.5 kcal mol^{-1} includes the proton translational energy $(3/2)RT$ and $PV = RT$.[52] The term ΔZPE is the zero point energy difference for the deprotonated state (A^-) minus the protonated state (AH), and it was estimated as ΔZPE = −7.6 and −7.9 kcal mol^{-1} for the OH^-/H_2O and the $Tyr237^-$/Tyr237 systems, respectively, by only optimizing the geometries (and then performing frequency calculations) of an OH^- and an H_2O molecule and the linked His233−Tyr237 side chains in both neutral and anionic His233−$Tyr237^-$ forms within the COSMO solvation model (with ε = 18.5 and all-electron/all-TZP basis set). Similarly, we also obtained ΔZPE = −8.1 kcal mol^{-1} for the His376 side chain to estimate its pK_a in section 3.4.

DOI: 10.1021/acs.inorgchem.5b00700
Inorg. Chem. 2015, 54, 7272−7290

Table 2. Calculated Properties for the Reduced $Fe^{2+}\cdots Cu^{+}$(Y237/Y237^{-}) DNC Models Generated Starting from the DNCs of 3EH5, 3EH3, and 1EHK X-ray Crystal Structures[a]

		geometry									net spin		$^{57}Fe^{2+}$ Mössbauer	
starting structure	models[b]	Fe−N (H384)	Fe···Cu	Cu−N (H233)	Cu−N (H282)	Cu−N (H283)	O···O (Y237)	E	pK_a (Y237)	Q	Fe^{2+}	Cu^{+}	δ	ΔE_Q
3EH5	$Fe^{2+,LS}\cdots Cu^{+}$ (Y237)	1.96	5.74	1.99	2.08	2.03	3.34	−41.8	7.0	0	0.00	0.00	0.64	2.43
	$Fe^{2+,IS}\cdots Cu^{+}$ (Y237)	2.38	5.48	2.00	2.07	2.04	3.43	−50.3	9.0	0	2.31	0.00	0.73	2.02
	$Fe^{2+,HS}\cdots Cu^{+}$ (Y237)	2.22	5.62	2.00	2.08	2.04	3.33	−49.6	7.8	0	3.90	0.00	0.92	2.21
	$Fe^{2+,LS}\cdots Cu^{+}$ (Y237^{-})	1.95	5.82	1.99	2.08	2.04	2.82	−47.1		−1	0.00	0.00	0.64	2.41
	$Fe^{2+,IS}\cdots Cu^{+}$ (Y237^{-})	2.34	5.55	1.99	2.08	2.04	2.80	−52.9		−1	2.32	0.00	0.73	2.08
	$Fe^{2+,HS}\cdots Cu^{+}$ (Y237^{-})	2.21	5.73	1.99	2.09	2.04	2.80	−53.8		−1	3.91	0.00	0.91	2.16
3EH3[c]	$Fe^{2+,HS}\cdots Cu^{+}$ (Y237^{-})	2.39	5.06	2.03	2.28	1.99	2.75	−38.6		−1	3.85	0.00	0.92	2.44
1EHK[d]	$Fe^{2+,HS}\cdots Cu^{+}$ (Y237^{-})$^{(1)}$	3.00	5.09	2.03	2.08	2.03	2.67	−31.5		−1	3.86	0.00	0.90	2.90
	$Fe^{2+,HS}\cdots Cu^{+}$ (Y237^{-})$^{(2)}$	2.71	5.36	2.02	2.10	2.03	2.68	−37.8		−1	3.87	0.00	0.94	2.67
	$Fe^{2+,HS}\cdots Cu^{+}$ (Y237^{-})$^{(3)}$	2.45	5.59	2.02	2.11	2.04	2.70	−42.4		−1	3.88	0.00	0.96	2.43
	$Fe^{2+,HS}\cdots Cu^{+}$ (Y237^{-})$^{(4)}$	2.33	5.74	2.02	2.10	2.04	2.70	−44.4		−1	3.89	0.00	0.96	2.34

[a]The properties include geometries (Å), electronic energies (E, offset by −25100 kcal mol^{-1}) obtained from the all-electron/all-TZP single-point energy calculations on the optimized geometries, pK_a's, the net charge (Q) of the clusters, Mulliken net spin polarizations for the Fe and Cu sites, and the ^{57}Fe Mössbauer isomer shifts (δ, mm s^{-1}) and quadrupole splittings (ΔE_Q, mm s^{-1}). [b]LS, low-spin; IS, intermediate-spin; HS, high-spin. [c]The Cartesian coordinates of N(His384), Fe, and Cu were fixed during geometry optimization. [d]Here, we deleted the bridging oxygen atom from the 1EHK structure, and geometry optimized the DNC cluster to see how the Fe···N(His384) distance and the Mössbauer properties will change. The $Fe^{2+,HS}\cdots Cu^{+}$(Y237^{-})$^{(1)}$, $Fe^{2+,HS}\cdots Cu^{+}$(Y237^{-})$^{(2)}$, and $Fe^{2+,HS}\cdots Cu^{+}$(Y237^{-})$^{(3)}$ are three points along the geometry optimization pathway. $Fe^{2+,HS}\cdots Cu^{+}$(Y237^{-})$^{(4)}$ is the lowest energy structure obtained.

3. RESULTS AND DISCUSSION OF FE^{2+}/CU^{+} REDUCED STATE DNC MODEL CALCULATIONS

3.1. $Fe^{2+}\cdots Cu^{+}$ DNC Calculations—Models Taken from 3EH5, 3EH3, and 1EHK. Feasible Structure of the Second Observed $^{57}Fe_{a3}{}^{2+}$ Component? No substantial electron density was observed directly between the Fe and Cu sites in the DNC's of the chemically reduced X-ray crystal structures of 3EH5 and 3EH3.[12] To see if such a DNC will yield the Mössbauer properties observed for the reduced *Tt* ba_3 C*c*O, we first built up our $Fe^{2+}\cdots Cu^{+}$ DNC model (similar to Figure 2, but without the oxygen species between the Fe and Cu sites) based on the 3EH5 Cartesian coordinates. Both the $Fe^{2+}\cdots Cu^{+}$(Y237) (180 atoms with neutral Tyr237 side chain) and $Fe^{2+}\cdots Cu^{+}$(Y237^{-}) (179 atoms with deprotonated anionic Tyr237^{-} side chain) clusters were geometry optimized with Fe^{2+} in LS, IS, and HS states. The calculated properties of these DNC models, including the main geometric parameters (Å), energies (E, off set by −25100 kcal mol^{-1}), Mulliken net spin polarizations on Fe^{2+} and Cu^{+}, and the $^{57}Fe^{2+}$ Mössbauer isomer shifts (δ) and quadrupole splittings (ΔE_Q) are given in Table 2 (in the 3EH5 section).

For both the $Fe^{2+}\cdots Cu^{+}$(Y237) and $Fe^{2+}\cdots Cu^{+}$(Y237^{-}) cases, the $Fe^{2+,HS}$ and $Fe^{2+,IS}$ states yield similar electronic energies, which are much lower than the corresponding $Fe^{2+,LS}$ state energy. Further, the calculated Mössbauer properties of δ = 0.92 mm s^{-1} and ΔE_Q = 2.21 mm s^{-1} for the $Fe^{2+,HS}\cdots Cu^{+}$(Y237) state and δ = 0.91 mm s^{-1} and ΔE_Q = 2.16 mm s^{-1} for the $Fe^{2+,HS}\cdots Cu^{+}$(Y237^{-}) state agree very well with the observed Mössbauer properties (δ = 0.92 mm s^{-1}, ΔE_Q = 2.34 mm s^{-1}) of the second $^{57}Fe_{a3}{}^{2+}$ component (Figure 1). Conversely, the calculated Mössbauer isomer shifts (0.73 mm s^{-1}) for both the $^{57}Fe^{2+,IS}$ sites are too small compared with the observed δ = 0.92/0.95 mm s^{-1} values. Therefore, our Mössbauer property calculations support that the $^{57}Fe_{a3}{}^{2+}$ species observed in the Mössbauer experiments are in high-spin states. The OLYP potential may underestimate the energy gap between the $Fe^{2+,IS}$ and $Fe^{2+,HS}$ states. However, although not included in the present calculations, both vibrational entropy and vibrational zero-point-energy terms most likely favor the $Fe^{2+,HS}$ state over the $Fe^{2+,IS}$ state. The Fe^{2+} site of the reduced DNC of ba_3 C*c*O in *Tt* then most likely exists only in the high-spin state at the *Thermus* optimum growth temperature of 50−80 °C.[53] We will therefore only report the results of the $Fe^{2+,HS}$ state for the rest of the reduced-DNC calculations in the current study.

For comparison, the experimental Mössbauer δ and ΔE_Q values for the reduced $^{57}Fe_{a3}{}^{2+}$ sites in c_1aa_3 from *Tt*[54] and aa_3 from a bovine heart[55] are also given in Table 1. The observed δ values for all $Fe_{a3}{}^{2+}$ sites are similar (0.92−0.96 mm s^{-1}) and are >0.9 mm s^{-1}, indicating they all are in the high-spin state. The ΔE_Q value for the $^{57}Fe_{a3}{}^{2+}$ in c_1aa_3 *Tt* (2.05 mm s^{-1}) is close to the second ΔE_Q (2.34 mm s^{-1}) observed in ba_3 *Tt*. These two may have very similar DNC structural features.

From the Mössbauer property calculations, one cannot tell under the conditions of the Mössbauer experiments whether the Tyr237 side chain is in a neutral or deprotonated anionic state. Taking E[$Fe^{2+,HS}\cdots Cu^{+}$(Y237^{-})] and E[$Fe^{2+,HS}\cdots Cu^{+}$(Y237)] from Table 2 for the E(A^{-}) and E(AH) terms in eq 4, we then obtained the pK_a(Y237) = 7.8. Because this

DOI: 10.1021/acs.inorgchem.5b00700
Inorg. Chem. 2015, 54, 7272−7290

calculated pK_a value is close to 7, considering the uncertainty of DFT calculations, the limited size of the quantum cluster model, and the fact that the pK_a calculations are for the equilibrium state at room temperature, it is not certain whether the Tyr237 side chains of the $Fe^{2+}\cdots Cu^{+}$-type DNC's are in a neutral or anionic state.

The experimental H-bonding O···O distance between the Tyr237 side chain and the geranyl −OH of the a_3-heme is only 2.61 Å in the X-ray crystal structure of 3EH5 (2.8 Å resolution). The DFT OLYP calculations predict 2.80 Å and a longer 3.33 Å for this O···O distance in the $Fe^{2+,HS}\cdots Cu^{+}(Y237^{-})$ and $Fe^{2+,HS}\cdots Cu^{+}(Y237)$ states, respectively. Therefore, the geometry optimization calculations support that the Tyr237 side chain in the X-ray crystal structure of 3EH5 is in anionic deprotonated state.

So far, our calculations show that the DNC of the second (minority) $Fe_{a3}{}^{2+}$ component observed in the Mössbauer experiment may have the $Fe^{2+,HS}\cdots Cu^{+}(Y237^{-}/Y237)$ structure. Now the question is, what is the DNC structure of the first (majority) $Fe_{a3}{}^{2+}$ component observed in the Mössbauer experiment?

We noticed that the DNC of 3EH3 is similar to that of 3EH5 but with a longer Fe−N(His384) distance (2.39 Å in 3EH3 relative to 2.10 Å in 3EH5 and 2.21 Å in the OLYP-optimized $Fe^{2+,HS}\cdots Cu^{+}(Y237^{-})$ structure). Next, we would examine how a longer Fe−N(His384) and a shorter $Fe^{2+,HS}\cdots Cu^{+}$ distance (5.06 Å in 3EH3 relative to 5.73 Å in the OLYP-optimized $Fe^{2+,HS}\cdots Cu^{+}(Y237^{-})$) will affect the $^{57}Fe^{2+}$ Mössbauer spectra, and if such a $Fe^{2+,HS}\cdots Cu^{+}$ DNC in 3EH3 would represent the first $Fe_{a3}{}^{2+}$ component observed in the Mössbauer experiment.

A new $Fe^{2+}\cdots Cu^{+}(Y237^{-})$ model was then constructed based on the DNC coordinates in 3EH3. Because we wanted to keep the Fe−N(His384) (2.39 Å in 3EH3) and $Fe^{2+,HS}\cdots Cu^{+}$ (5.06 Å in 3EH3) distances, the atom positions of N(His384), Fe, and Cu were fixed during geometry optimization. Then, the Mössbauer property calculation on this partially optimized 3EH3-$Fe^{2+,HS}\cdots Cu^{+}(Y237^{-})$ model yielded δ = 0.92 mm s^{-1} and ΔE_Q = 2.44 mm s^{-1} (also given in Table 2, 3EH3 section), which is similar to the Mössbauer parameters of δ = 0.91 mm s^{-1} and ΔE_Q = 2.16 mm s^{-1} obtained for the 3EH5-$Fe^{2+,HS}\cdots Cu^{+}(Y237^{-})$ model. Because the experimentally observed component 1 of $^{57}Fe_{a3}{}^{2+}$ has a smaller ΔE_Q = 1.43 mm s^{-1},[18] whereas the model 3EH3-$Fe^{2+,HS}\cdots Cu^{+}(Y237^{-})$ yields an even larger ΔE_Q = 2.44 mm s^{-1}, this 3EH3-$Fe^{2+,HS}\cdots Cu^{+}(Y237^{-})$ model does not represent the DNC structure of the first $Fe_{a3}{}^{2+}$ component observed in the Mössbauer experiment.

As mentioned earlier in 1EHK, the axial His384 side chain was farther away from the Fe atom with the Fe···N(His384) distance of 3.31 Å. An oxygen species (probably originating from the oxidized state) was found between the Fe and Cu sites. To see if this long Fe···N(His384) distance will remain and how it affects the $^{57}Fe^{2+}$ Mössbauer properties when the bridging oxygen species is omitted, we took the DNC model (Figure 2) from 1EHK, deleted the bridging oxygen atom, and optimized the geometry in the $Fe^{2+,HS}\cdots Cu^{+}(Y237^{-})$ state. The geometric and Mössbauer properties of the three structures $Fe^{2+,HS}\cdots Cu^{+}(Y237^{-})^{(1-3)}$ along the optimization trajectory and the final optimized structure $Fe^{2+,HS}\cdots Cu^{+}(Y237^{-})^{(4)}$ are also shown in Table 2 (in the 1EHK section). Without the bridging oxygen species, the $Fe^{2+,HS}$ and the Cu^{+} sites move away from each other during the geometry optimization. The Fe··· N(His384) distance is gradually shortened, and because the His384 side chain cannot move freely (H_{link} is fixed during geometry optimization), Fe^{2+} moves toward the N(His384) atom. The final structure $Fe^{2+,HS}\cdots Cu^{+}(Y237^{-})^{(4)}$ is 9.4 kcal mol^{-1} higher in energy than that of the 3EH5-$Fe^{2+,HS}\cdots Cu^{+}(Y237^{-})$ optimized geometry.

The calculated Mössbauer properties on $Fe^{2+,HS}\cdots Cu^{+}(Y237^{-})^{(1-4)}$ show that when the Fe···N(His384) distance is very long (3.0 Å), the calculated Mössbauer isomer shift is relatively smaller (δ = 0.90 mm s^{-1}), and the quadrupole splitting value is very large (ΔE_Q = 2.90 mm s^{-1}). As the Fe··· N(His384) distance gets shorter, the calculated δ gets larger and ΔE_Q becomes smaller. Therefore, the $Fe^{2+,HS}\cdots Cu^{+}(Y237^{-})$ model with a long Fe···N(His384) distance does not represent the DNC structure of the experimentally observed component one, which has a large δ = 0.95 mm s^{-1} and a small ΔE_Q = 1.43 mm s^{-1}.[18]

Next, we study whether the bridging oxygen species in 1EHK is H_2O or OH^{-} and if the Fe^{2+}-H_2O-Cu^{+}/Fe^{2+}-OH^{-}-Cu^{+} structures will yield the Mössbauer properties of the first $^{57}Fe_{a3}{}^{2+}$ component observed in the Mössbauer experiment.

3.2. Bridging H_2O (Fe^{2+}-H_2O-Cu^{+}) or OH^{-} (Fe^{2+}-OH^{-}-Cu^{+}) in the DNC of 1EHK? From the X-ray crystal structure, the Tyr237 side chain in 1EHK is also likely in the deprotonated anionic state because the H-bonding O···O distance between the Tyr237 side chain and the geranyl −OH of the a_3-heme is only 2.52 Å. Therefore, we optimized the geometry of the 1EHK-$Fe^{2+,HS}$-H_2O-$Cu^{+}(Y237^{-})$ DNC cluster (Figure 2, starting with bridging H_2O) with the deprotonated $Tyr237^{-}$ side chain. The calculated geometrical parameters of the DNC, the energy (E), and the $^{57}Fe^{2+}$ Mössbauer properties are given in Table 3.

In 1EHK, the Fe···Cu distance is very short (4.40 Å); the distance of Fe−O (2.26 Å) is similar to the distance of Cu−O (2.31 Å), and the bridging O is close to the line connecting the Fe and Cu sites with ∠Fe-O-Cu = 148°. During DFT geometry optimization, the proposed bridging H_2O molecule gradually moves away from both the Fe^{2+} and Cu^{+} sites, and finally detaches from them. The Fe^{2+} and Cu^{+} sites also move apart from each other. The final Fe···O, Cu···O, and Fe···Cu distances are 2.41, 3.57, and 5.26 Å, respectively. Therefore, the H_2O molecule does not bind with either the $Fe^{2+,HS}$ or Cu^{+} site. The bridging oxygen species in 1EHK is therefore probably not a water molecule.

The central portion of the optimized $Fe^{2+,HS}$-H_2O-$Cu^{+}(Y237^{-})$ geometry is shown in Figure S1 in the Supporting Information. Although the H_2O molecule is 2.41 Å away from the $Fe^{2+,HS}$ site, it prevents the $Fe^{2+,HS}$ from moving toward the His384 side chain. Without this H_2O molecule (see section 3.1 and $Fe^{2+,HS}\cdots Cu^{+}(Y237^{-})^{(4)}$ in Table 2), $Fe^{2+,HS}$ would bind to His384, and the calculated Fe···N(His384) distance would be shortened to 2.33 Å. This H_2O molecule only moderately affects the Mössbauer properties of $^{57}Fe^{2+,HS}$. From 3EH5-$Fe^{2+,HS}\cdots Cu^{+}(Y237^{-})$ (see Table 2) to the current 1EHK-$Fe^{2+,HS}$-H_2O-$Cu^{+}(Y237^{-})$, the calculated isomer shift decreases from 0.91 to 0.90 mm s^{-1}, and the quadrupole splitting increases from 2.16 to 2.60 mm s^{-1}. Overall, the δ = 0.90 mm s^{-1} and ΔE_Q = 2.60 mm s^{-1} values are still in reasonable agreement with the experimental results (the second $^{57}Fe_{a3}{}^{2+}$ component) of δ = 0.92 mm s^{-1} and ΔE_Q = 2.34 mm s^{-1}. It is not clear if there is a water molecule trapped in the DNC of the enzyme under the conditions of the Mössbauer experiments.

To test if an OH^{-} would stay in the bridging position of the oxygen species found in the DNC of 1EHK, we also geometry optimized the 1EHK-$Fe^{2+,HS}$-OH^{-}-$Cu^{+}(Y237^{-})$ model. The

DOI: 10.1021/acs.inorgchem.5b00700
Inorg. Chem. 2015, 54, 7272−7290

Table 3. Calculated Properties of the Reduced $Fe^{2+,HS}$-H_2O-$Cu^+(Y237^-)$ Model with Bridging H_2O and $Fe^{2+,HS}$-OH^--$Cu^+(Y237^-/Y237)$ Models with Bridging OH^- Generated from the DNC of the 1EHK X-ray Crystal Structure[a]

	geometry											net spin		$^{57}Fe^{2+}$ Mössbauer	
state	Fe–N (H384)	Fe–O	Cu–O	∠Fe–O–Cu	Fe···Cu	Cu–N (H233)	Cu–N (H282)	Cu–N (H283)	O···O (Y237)	E	pK_a (Y237)	pK_a (H_2O)	Q	Fe^{2+}	Cu^+	δ	ΔE_Q
$Fe^{2+,HS}$-H_2O-$Cu^+(Y237^-)$	3.15	2.41	3.57	122	5.26	2.01	2.10	2.04	2.72	−357.7		17.3	−1	3.86	0.00	0.90	2.60
$Fe^{2+,HS}$-OH^--$Cu^+(Y237^-)$	4.07	1.95	2.31	135	3.95	2.11	2.15	2.16	2.73	−349.2			−2	3.90	0.05	0.80	1.82
$Fe^{2+,HS}$-OH^--$Cu^+(Y237)$	4.17	1.94	2.39	138	4.05	2.10	2.14	2.14	3.15	−352.3	13.1		−1	3.88	0.03	0.80	1.89
exp. (1EHK)[b]	3.31	2.26	2.31	148	4.40	2.10	2.21	2.13	2.52								

[a]The properties include geometries (Å, °), electronic energies (E, offset by −25100 kcal mol^{-1}) obtained from the all-electron/all-TZP single-point energy calculations on the optimized geometries, pK_a's, the net charge (Q) of the clusters, Mulliken net spin polarizations for the Fe and Cu sites, and the ^{57}Fe Mössbauer isomer shifts (δ, mm s^{-1}) and quadrupole splittings (ΔE_Q, mm s^{-1}). [b]A bridging oxygen species was found in between the Fe and Cu sites in the DNC of the radiation-reduced X-ray crystal structure of 1EHK (2.4 Å resolution).[10] Here we study if this bridging oxygen species is a H_2O molecule or a hydroxide anion.

OH^- clearly stays in the bridging position. The optimized structure is given in Figure S2 in the Supporting Information. The calculated Fe–O (1.95 Å) and Cu–O (2.31 Å) distances in this model (see Table 3) are much closer to the corresponding distances (2.26 and 2.31 Å) in 1EHK than in the calculated $Fe^{2+,HS}$-H_2O-$Cu^+(Y237^-)$ model. Therefore, the bridging oxygen species in 1EHK is better represented by a hydroxide anion than by a water molecule.

The optimized $Fe^{2+,HS}$-OH^--$Cu^+(Y237^-)$ structure has a shorter Fe···Cu distance and a longer Fe···N(His384) distance compared to the X-ray crystal structure (1EHK). The radiolyticly reduced protein is likely not in an equilibrium state. The structure 1EHK may represent a mixture of the $Fe^{2+,HS}$-OH^--$Cu^+(Y237^-)$ and the open $Fe^{2+,HS}$···$Cu^+(Y237^-)$ states (Table 2). A minority contribution from $Fe^{2+,HS}$-H_2O-$Cu^+(Y237^-)$ to 1EHK is also possible.

We further optimized the geometry of the $Fe^{2+,HS}$-OH^--$Cu^+(Y237)$ state with neutral Tyr237; its calculated properties are provided in Table 3. Because the calculated pK_a for the Tyr237 side chain is 13.1, the Tyr237 energetically favors the neutral protonated form in the equilibrium state at room temperature. Further, comparing tautomers, the energy of $Fe^{2+,HS}$-H_2O-$Cu^+(Y237^-)$ is 5.4 kcal mol^{-1} lower than that of the $Fe^{2+,HS}$-OH^--$Cu^+(Y237)$ state, indicating that $Fe^{2+,HS}$-H_2O-$Cu^+(Y237^-)$ is energetically more stable than the $Fe^{2+,HS}$-OH^--$Cu^+(Y237)$ state, and therefore also more stable than the $Fe^{2+,HS}$-OH^--$Cu^+(Y237^-)$ state. This conclusion is also supported by the calculated pK_a value of 17.3 for the H_2O molecule in $Fe^{2+,HS}$-H_2O-$Cu^+(Y237^-)$. Therefore, the radiolyticly reduced DNC of $Fe^{2+,HS}$-OH^--$Cu^+(Y237^-)$ in 1EHK is not in an equilibrium state. The bridging OH^- is likely trapped, originating from 2e$^-$ reduction of the oxidized Fe^{3+}-OH^--$Cu^{2+}(Y237^-)$ state at low temperature with an effective kinetic barrier to proton transfer from the K-path.

The $Fe^{2+,HS}$-OH^--$Cu^+(Y237^-)$ and $Fe^{2+,HS}$-OH^--$Cu^+(Y237)$ clusters yield essentially the same Mössbauer isomer shift (0.80 mm s^{-1}) and quadrupole splitting (1.82/1.89 mm s^{-1}) properties. Compared with the open $Fe^{2+,HS}$···$Cu^+(Y237^-/Y237)$ structures in Table 2, the bridging OH^- in $Fe^{2+,HS}$-OH^--$Cu^+(Y237^-/Y237)$ lowers both the $^{57}Fe^{2+,HS}$ Mössbauer isomer shift and quadrupole splitting values. Because the calculated δ = 0.80 mm s^{-1} is well below the observed values of 0.92/0.95 mm s^{-1}, the radiolyticly reduced $Fe^{2+,HS}$-OH^--$Cu^+(Y237^-)$ DNC in 1EHK does not represent either Fe_{a3}^{2+} component observed in the Mössbauer experiments.

3.3. Terminal H_2O or OH^- in the DNC of 3EH4? As mentioned earlier, in the radiolyticly reduced X-ray crystal structures 3EH4 and 1XME (Table 1), the oxygen species found in the DNC is much closer to the Cu^+ site. We now start from the DNC of 3EH4 to study whether a water molecule or an OH^- can be terminally bound to the Cu^+ site. We geometry optimized the $Fe^{2+,HS}$···H_2O-$Cu^+(Y237^-/Y237)$ and $Fe^{2+,HS}$···OH^--$Cu^+(Y237^-/Y237)$ DNC clusters in both anionic $Tyr237^-$ and neutral Tyr237 states and also calculated the $^{57}Fe^{2+,HS}$ Mössbauer properties. The calculated results are given in Table 4.

As shown in Figure 3, during geometry optimizations, the Cu^+-terminally bound H_2O molecule in both $Fe^{2+,HS}$···H_2O-$Cu^+(Y237^-/Y237)$ models dissociated from the Cu^+ site. It stayed in between Fe^{2+} and Cu^+ but did not bind to either site. Therefore, the oxygen species observed in the DNC of 3EH4 cannot be a water molecule.

DOI: 10.1021/acs.inorgchem.5b00700
Inorg. Chem. 2015, 54, 7272−7290

Table 4. Calculated Properties of the Reduced $Fe^{2+,HS}$···H_2O-Cu^+(Y237$^-$/Y237) and $Fe^{2+,HS}$···OH^--Cu^+(Y237$^-$/Y237) DNC Models Generated from the DNC of the X-ray Crystal Structure of 3EH4[a]

	geometry											net spin		$^{57}Fe^{2+}$ Mössbauer	
state	Fe–N (H384)	Fe···O	Cu–O	∠Fe–O–Cu	Fe···Cu	Cu–N (H233)	Cu–N (H282)	Cu–N (H283)	O···O (Y237)	E	pK_a (Y237)	pK_a (H_2O)	Q	Fe^{2+}	Cu^+	δ	ΔE_Q
$Fe^{2+,HS}$···H_2O-Cu^+(Y237$^-$)	2.17	4.05	3.30	100	5.65	1.99	2.11	2.01	2.81	−366.5		27.4	−1	3.88	0.00	0.91	2.31
$Fe^{2+,HS}$···H_2O-Cu^+(Y237)	2.18	3.93	3.25	104	5.68	2.00	2.09	2.04	3.29	−366.8	11.1	25.0	0	3.88	0.00	0.91	2.20
$Fe^{2+,HS}$···OH^--Cu^+(Y237$^-$)	2.22	4.01	1.95	113	5.10	2.18	2.07	2.29	2.89	−344.2			−2	3.83	0.28	0.93	1.01
$Fe^{2+,HS}$···OH^--Cu^+(Y237)	2.22	3.82	1.93	116	4.98	2.31	2.02	2.42	3.29	−347.7	13.4		−1	3.84	0.23	0.92	1.20
exp. (3EH4)[b]	2.39	3.08	2.20	126	4.73	1.96	2.03	1.97	2.47								

[a]The properties include geometries (Å, °), electronic energies (E, offset by −25100 kcal mol^{-1}) obtained from the all-electron/all-TZP single-point energy calculations on the optimized geometries, pK_a's, the net charge (Q) of the clusters, Mulliken net spin polarizations for the Fe and Cu sites, and the ^{57}Fe Mössbauer isomer shifts (δ, mm s^{-1}) and quadrupole splittings (ΔE_Q, mm s^{-1}). [b]An oxygen species between the Fe^{2+} and Cu^+ sites but much closer to the Cu^+ site was observed in the DNC of the X-ray crystal structure of 3EH4 (2.9 Å resolution).[12] Here we study if this oxygen species is a terminally bound (to Cu^+) H_2O molecule or a hydroxide anion.

The optimized $Fe^{2+,HS}$···H_2O-Cu^+(Y237$^-$/Y237) clusters yield very similar $^{57}Fe^{2+,HS}$ Mössbauer properties (δ = 0.91 mm s^{-1}, ΔE_Q = 2.31/2.20 mm s^{-1}), which are very close to the calculated $^{57}Fe^{2+,HS}$ Mössbauer properties (δ = 0.91/0.92 mm s^{-1}, ΔE_Q = 2.16/2.21 mm s^{-1}) for the open $Fe^{2+,HS}$··· Cu^+(Y237$^-$/Y237) structures calculated for the 3EH5 DNC (see Table 2) and are also consistent with the second $^{57}Fe_{a3}{}^{2+}$ component (δ = 0.92 mm s^{-1}, ΔE_Q = 2.34 mm s^{-1}) observed in the Mössbauer experiments.[18]

Although this dangling H_2O molecule between the Fe^{2+} and Cu^+ sites has little effect on the $^{57}Fe^{2+,HS}$ Mössbauer properties, it does affect the pK_a of the Tyr237 side chain. The Fe^{2+}···Cu^+ distance is very similar with or without the weak H_2O bridge. Here, with a water molecule in the DNC, the pK_a of the Tyr237 side chain is estimated as 11.1, which is a 3.3-unit increase from the corresponding calculated pK_a (7.8) for the 3EH5 open DNC $Fe^{2+,HS}$···Cu^+(Y237$^-$/Y237) models in Section 3.1 (Table 2). The sensitivity of the pK_a of this unique Tyr237 residue in response to this structural and component change in the DNC is suggestive of a potential role in proton transfer and proton pumping during the catalytic cycle. For example, proton transfer from Tyr237 toward the reaction center or above it could be promoted in the "open" form.

By contrast, during geometry optimizations, the terminally bound OH^- in both $Fe^{2+,HS}$···OH^--Cu^+(Y237$^-$/Y237) clusters remained tightly bound to the Cu^+ site (see Figure 4). In these two optimized geometries, the Fe···O and Fe···Cu distances are longer and the Fe–N(His384) and Cu–O distances are shorter than the corresponding values in the radiolyticly reduced X-ray crystal structure 3EH4. It is possible that the DNC of 3EH4 represents a mixture of the structures $Fe^{2+,HS}$···OH^--Cu^+(Y237$^-$), $Fe^{2+,HS}$···Cu^+(Y237$^-$), and/or $Fe^{2+,HS}$-OH^--Cu^+(Y237$^-$) (bridging OH^-).

The $Fe^{2+,HS}$···OH^--Cu^+(Y237$^-$/Y237) states also yield very similar Mössbauer properties (δ = 0.93/0.92 mm s^{-1}, ΔE_Q = 1.01/1.20 mm s^{-1}), which are so far the closest calculated results to the majority first $^{57}Fe_{a3}{}^{2+}$ component property (δ = 0.95 mm s^{-1}, ΔE_Q = 1.43 mm s^{-1}) observed in Mössbauer experiments.[18]

The calculated pK_a (27.4/25.0) of the H_2O molecule in the DNC and the pK_a (11.1/13.4) of the Tyr237 side chain indicate that, when there is an oxygen species in between the $Fe^{2+,HS}$ and Cu^+ sites, the $Fe^{2+,HS}$···Cu^+ DNC strongly favors a H_2O molecule at thermodynamic equilibrium rather than a hydroxide anion, and the Tyr237 side chain energetically prefers the protonated charge-neutral state. In 3EH4, the O···O distance between the Tyr237 side chain and the geranyl –OH of the a_3-heme is very short (2.47 Å). It is likely that the Tyr237 side chain in 3EH4 is in the deprotonated anionic state. Therefore, the Fe^{2+}···OH^--Cu^+(Y237$^-$) DNC structure of 3EH4 probably originates from the oxidized state. That is, if the oxidized as-isolated DNC has a structure like Fe^{3+}···OH^--Cu^{2+}(Y237$^-$) when it is radiolyticly reduced by the X-ray beam at low temperature with limited proton mobility, the Cu-bound OH^- is then trapped in the reduced state, and the Tyr237 side chain remains in the anionic state.

However, comparing the optimized geometries of the $Fe^{2+,HS}$···OH^--Cu^+(Y237$^-$) and $Fe^{2+,HS}$···OH^--Cu^+(Y237) states (in Table 4), we notice that, in $Fe^{2+,HS}$···OH^--Cu^+(Y237), both the Cu–O and Cu–N(H282) distances are shorter and both the Cu–N(H233) and Cu–N(H283) distances are longer than the corresponding Cu-ligand distances in $Fe^{2+,HS}$···OH^--Cu^+(Y237$^-$). In other words, upon proto-

DOI: 10.1021/acs.inorgchem.5b00700
Inorg. Chem. 2015, 54, 7272–7290

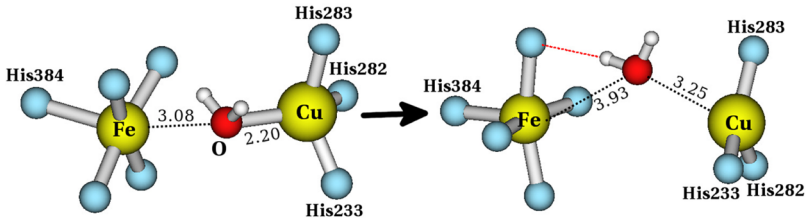

Figure 3. Left: The central portion of the initial $Fe^{2+,HS}\cdots H_2O$-Cu^+(Y237$^-$/Y237) structure, which was taken from the DNC of the 3EH4 X-ray crystal structure. Right: During geometry optimizations, the H_2O molecule dissociated from the Cu^+ site. Distances (Å) on the right are taken from the optimized $Fe^{2+,HS}\cdots H_2O$-Cu^+(Y237) structure.

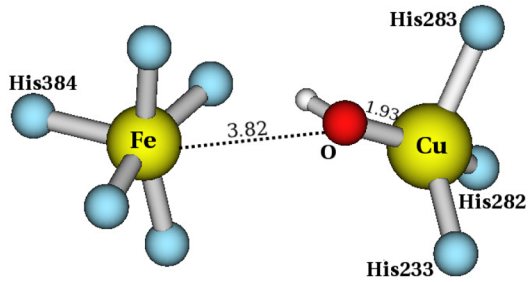

Figure 4. Central portion of the optimized $Fe^{2+,HS}\cdots OH^-$-Cu^+(Y237) structure with OH^- binding with Cu^+. Labeled distances are in Å.

nation of the Tyr237 side chain, the OH^- ligand will bind even stronger with Cu^+. Therefore, even when Tyr237 is protonated in the $Fe^{2+,HS}\cdots OH^-$-Cu^+ state, because of the proton transfer barrier from neutral Tyr237 to the OH^--Cu^+, the $Fe^{2+,HS}\cdots OH^-$-Cu^+(Y237) state may still be trapped at low temperature in the Mössbauer experimental conditions.

3.4. Changing of the Cu^+ Coordination State and Feasible DNC Structure of the first $^{57}Fe_{a3}{}^{2+}$ Component Observed in the Mössbauer Experiments. The overall charge of the $Fe^{2+,HS}\cdots OH^-$-Cu^+(Y237) quantum cluster is −1, whereas the total charge of the $Fe^{2+,HS}\cdots H_2O$-Cu^+(Y237) state is 0. It is also possible that the $Fe^{2+,HS}\cdots OH^-$-Cu^+(Y237) state is stabilized by an extra proton in the proton loading site (PLS), which is close to the DNC. It is still not known where the PLS exactly locates in the ba_3 C*c*O from *Tt*. For simplicity, Fee et al. protonated the His376 side chain (the positive imidazolium form) to represent having a proton at the PLS.[17,42] According to Gennis and co-workers' mutagenesis and kinetics studies of proton pumping in ba_3 C*c*O from *Tt*, His376 is probably close to the proton exit path but not absolutely required.[56] However, to compare how the energy changes when an extra proton exists in the $Fe^{2+,HS}\cdots OH^-$-Cu^+(Y237) cluster, starting from the optimized $Fe^{2+,HS}\cdots OH^-$-Cu^+(Y237) structure, we also protonated the His376 side chain and performed geometry optimization calculations. This His376-protonated cluster is named $Fe^{2+,HS}\cdots OH^-$-Cu^+(Y237)(H376H$^+$). Interestingly, we observed that during the geometry optimization the His283 side chain gradually tilted up and dissociated from the Cu^+ site, and the Cu^+ changed from 4-coordinate (4c) state to 3-coordinate (3c) configuration. In the meantime, the His233 side chain also slowly moved away from the Cu^+, and both the OH^- ligand and the His282 side chain were closer to the Cu^+. Finally, the His233 side chain also dissociated from Cu^+, and the optimized structure ended with a 2-coordinate (2c) Cu^+ site with a near-linear OH^--Cu^+_{2c}-N(His282) configuration (see Figure 5). The calculated properties of this structure are given in the first row of Table 5 (footnote b). Its relative energy (−364 kcal mol^{-1}) is very close to that (−366.8 kcal mol^{-1}) of

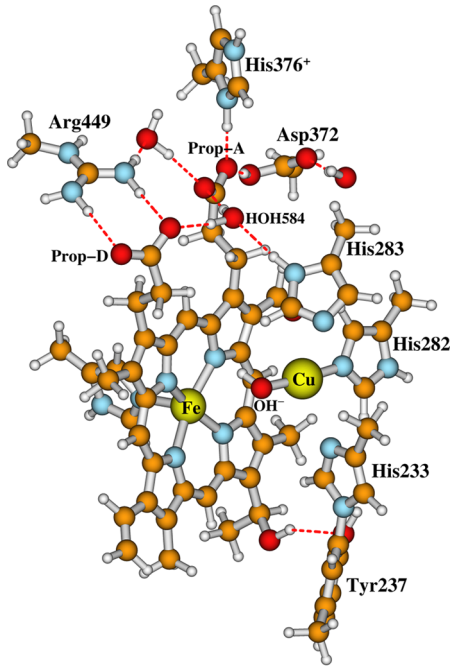

Figure 5. Optimized structure of the $Fe^{2+,HS}\cdots OH^-$-Cu^+_{2c}(Y237)-(H376H$^+$) cluster with a neutral Tyr237 and a cationic protonated His376$^+$ side chain. During the geometry optimization process, the Cu^+ site changes from 4-coordinate to 2-coordinate (2c) configuration with both His283 and His233 side chains gradually dissociating from the Cu^+.

the $Fe^{2+,HS}\cdots H_2O$-Cu^+(Y237) state (in Table 4). These two tautomers are therefore close in energy but differ strongly in Cu^+ coordination geometry and proton location.

We then deleted the added proton on His376$^+$ and optimized the geometry to obtain the $Fe^{2+,HS}\cdots OH^-$-Cu^+_{2c}(Y237) structure with the 2-coordinated Cu^+. The calculated properties of the optimized $Fe^{2+,HS}\cdots OH^-$-Cu^+_{2c}(Y237) cluster are given in the second row of Table 5 (footnote c). During the geometry optimization, the Fe···Cu, Cu···N(His233), and Cu···N(His283) distances are lengthened further. However, overall, the geometries of the optimized $Fe^{2+,HS}\cdots OH^-$-Cu^+_{2c}(Y237)(H376H$^+$) and $Fe^{2+,HS}\cdots OH^-$-Cu^+_{2c}(Y237) structures are very similar. In both structures, the angle of OH^-−Cu−N(His282) is 176°, which is close to a linear structure. The relative energy of the $Fe^{2+,HS}\cdots OH^-$-Cu^+_{2c}(Y237) state is ∼17 kcal mol^{-1} lower than that of its corresponding 4-coordinate Cu^+ state $Fe^{2+,HS}\cdots OH^-$-Cu^+(Y237), as given in Table 4. Therefore, with OH^- binding to Cu^+, the DNC favors the 2-coordinate Cu^+ structure. The calculated Mössbauer properties of both the $Fe^{2+,HS}\cdots OH^-$-

DOI: 10.1021/acs.inorgchem.5b00700
Inorg. Chem. 2015, 54, 7272−7290

Table 5. Calculated Properties for the DNC Models with a 3- or 2- Coordinate (3c/2c) Cu^+ Site in which His233/His283 Dissociated from the Cu^+[a]

	geometry												net spin		$^{57}Fe^{2+}$ Mössbauer	
state	Fe−N (H384)	Fe···O	Cu−O	∠Fe−O−Cu	Fe···Cu	Cu−N (H233)	Cu−N (H282)	Cu−N (H283)	∠O−Cu−N (H282)	E	pK_a ($H376H^+$)	Q	Fe^{2+}	Cu^+	δ	ΔE_Q
$Fe^{2+,HS}$···OH^--Cu^+_{2c}(Y237) ($H376H^+$)[b]	2.20	3.95	1.85	101	4.66	3.02	1.90	4.03	176	−364.0	10.3	0	3.89	0.00	0.91	2.17
$Fe^{2+,HS}$···OH^--Cu^+_{2c}(Y237)[c]	2.19	4.19	1.86	97	4.78	3.09	1.90	4.25	176	−364.6		−1	3.89	0.00	0.91	2.28
$Fe^{2+,HS}$···OH^--Cu^+_{3c}(Y237) ($H376H^+$)$^{(1)}$[d]	2.21	3.86	1.92	113	4.94	2.32	2.00	2.60	160	−350.7	11.2	0	3.85	0.20	0.92	1.32
$Fe^{2+,HS}$···OH^--Cu^+_{3c}(Y237) ($H376H^+$)$^{(2)}$[d]	2.20	3.86	1.91	111	4.89	2.36	1.97	2.83	163	−352.8	11.2	0	3.86	0.15	0.92	1.51
$Fe^{2+,HS}$···OH^--Cu^+_{3c}(Y237) ($H376H^+$)$^{(3)}$[d]	2.21	3.82	1.89	110	4.80	2.44	1.95	3.09	166	−355.3	12.1	0	3.87	0.11	0.92	1.75
$Fe^{2+,HS}$···OH^--Cu^+_{2c}(Y237) ($H376H^+$)$^{(4)}$[d]	2.21	3.78	1.89	108	4.71	2.64	1.92	3.30	172	−356.9	10.8	0	3.88	0.04	0.91	2.02
$Fe^{2+,HS}$···OH^--Cu^+_{3c}(Y237)$^{(1)}$[e]	2.22	3.85	1.91	114	4.94	2.32	2.00	2.60	159	−350.0		−1	3.85	0.20	0.92	1.31
$Fe^{2+,HS}$···OH^--Cu^+_{3c}(Y237)$^{(2)}$[e]	2.21	3.85	1.90	112	4.89	2.36	1.97	2.83	162	−352.1		−1	3.86	0.15	0.92	1.52
$Fe^{2+,HS}$···OH^--Cu^+_{3c}(Y237)$^{(3)}$[e]	2.21	3.83	1.89	109	4.80	2.44	1.95	3.09	166	−353.4		−1	3.87	0.11	0.92	1.75
$Fe^{2+,HS}$···OH^--Cu^+_{2c}(Y237)$^{(4)}$[e]	2.21	3.77	1.87	108	4.71	2.64	1.92	3.30	171	−356.8		−1	3.88	0.04	0.92	2.06
$Fe^{2+,HS}$···H_2O-Cu^+_{3c}(Y237)[f]	2.19	4.19	2.35	106	5.35	1.99	1.94	4.45	132	−368.9		0	3.89	0.00	0.91	2.31
$Fe^{2+,HS}$···H_2O···Cu^+_{2c}(Y237)[f]	2.20	4.76	3.13	95	5.92	1.92	1.91	5.40		−378.7		0	3.88	0.00	0.91	2.24

[a]The properties include geometries (Å, °), electronic energies (E, offset by −25100 kcal mol^{-1}) obtained from the all-electron/all-TZP single-point energy calculations on the optimized geometries, pK_a's, the net charge (Q) of the clusters, Mulliken net spin polarizations for the Fe and Cu sites, and the ^{57}Fe Mössbauer isomer shifts (δ, mm s^{-1}) and quadrupole splittings (ΔE_Q, mm s^{-1}). [b]Both His233 and His283 side chains dissociated from the Cu^+ site during the geometry optimization. [c]After deleting the H^+ of $His376^+$ in $Fe^{2+,HS}$···OH^--Cu^+_{2c}(Y237)($H376H^+$), and geometry optimizing the structure, the Cu^+ site remained in the 2c configuration. [d]Four structures (1−4) with a 3c or 2c Cu^+ site, which were taken from the geometry optimization trajectory of the $Fe^{2+,HS}$···OH^--Cu^+_{2c}(Y237)($H376H^+$) state. [e]See footnote d above. These are the four corresponding structures of the $Fe^{2+,HS}$···OH^--Cu^+(Y237) state. [f]When protonating the OH^- ligand in $Fe^{2+,HS}$···OH^--Cu^+_{2c}(Y237) and optimizing the geometry, the Cu^+ coordination state changes from $Fe^{2+,HS}$···H_2O-Cu^+_{2c}(Y237) (left in Figure 7) to $Fe^{2+,HS}$···H_2O-Cu^+_{3c}(Y237) (middle in Figure 7) and to $Fe^{2+,HS}$···H_2O···Cu^+_{2c}(Y237) (right in Figure 7).

DOI: 10.1021/acs.inorgchem.5b00700
Inorg. Chem. 2015, 54, 7272−7290

$Cu^{+}_{2c}(Y237)(H376H^{+})$ and $Fe^{2+,HS}\cdots OH^{-}$-$Cu^{+}_{2c}(Y237)$ states (δ = 0.91 mm s^{-1}, ΔE_Q = 2.17/2.28 mm s^{-1}) are now similar to those of the open $Fe^{2+,HS}\cdots Cu^{+}(Y237^{-}/Y237)$ structures given in Table 2 and the structure with a dangling H_2O molecule (in Table 4) between the $Fe^{2+,HS}$ and Cu^{+} sites. In other words, the $Fe^{2+,HS}\cdots OH^{-}$-$Cu^{+}_{2c}(Y237)(H376H^{+})$ and $Fe^{2+,HS}\cdots OH^{-}$-$Cu^{+}_{2c}(Y237)$ states with 2-coordinate Cu^{+} do not represent the DNC of the first (majority) $^{57}Fe_{a3}{}^{2+}$ component observed in the Mössbauer experiments[18] but are entirely compatible with the observed second (minority) $^{57}Fe_{a3}{}^{2+}$ Mössbauer experimental parameters (δ = 0.92 mm s^{-1}, ΔE_Q = 2.34 mm s^{-1}).

Reviewing the X-ray crystal structure of 3EH4, we found that the side chain of Trp229 is very close (with the closest atom to atom distance being 3.4 Å) and parallel to the side chain of His283 (see Figure 6). During the $Cu^{+}_{4c} \rightarrow Cu^{+}_{2c}$ transition in

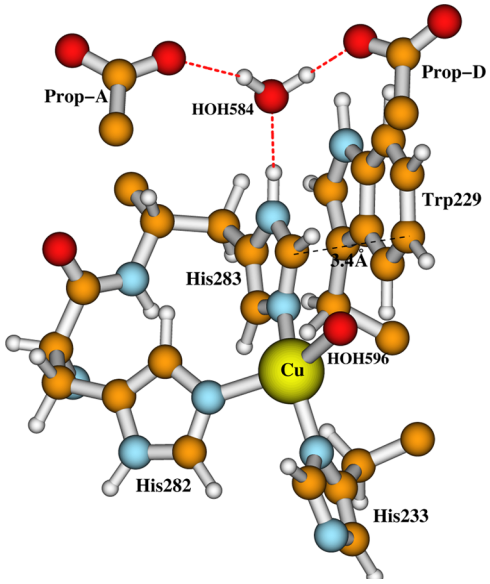

Figure 6. Taken from the X-ray crystal structure of 3EH4, which shows that the side chain of Trp229 is very close (with the closest atom to atom distance being 3.4 Å) and parallel to the side chain of His283. The steric interaction between the two side chains prevents His283 from freely moving away from the Cu^{+} site.

the geometry optimization of the $Fe^{2+,HS}\cdots OH^{-}$-$Cu^{+}(Y237)(H376H^{+})$ state, the side chain of His283 tilted up and away from the Cu^{+} and moved toward the side chain of Trp229 (not included in the current model calculation). Therefore, we propose that because of the steric interactions and the potential energy barriers encountered upon moving the His233 and His283 side chains away from Cu^{+}, the OH^{-}-Cu^{+} site is frequently trapped in the Cu^{+}_{4c} or Cu^{+}_{3c} configurations, particularly under the low temperature in Mössbauer experiments.

To test this idea, we picked four structures with a "maximum gradient" of <0.005 au/Å along the geometry optimization trajectory of $Fe^{2+,HS}\cdots OH^{-}$-$Cu^{+}(Y237)(H376H^{+})$ to represent the middle structures of the $Cu^{+}_{4c} \rightarrow Cu^{+}_{2c}$ transition. The calculated properties of the four $Fe^{2+,HS}\cdots OH^{-}$-$Cu^{+}_{3c/2c}(Y237)(H376H^{+})^{(1-4)}$ structures from all-electron/all-TZP single-point energy calculations are also given in Table 5 (rows 3–6 with footnote d). We noticed that the structural and coordination state of the Cu^{+} site indeed influences the electric field at the Fe^{2+} site and therefore affects the $^{57}Fe^{2+}$ Mössbauer, especially the quadruple splitting property. The Cu^{+}_{4c} structure of $Fe^{2+,HS}\cdots OH^{-}$-$Cu^{+}(Y237^{-})$ in Table 4 yields a large calculated isomer shift (0.93 mm s^{-1}) and a small quadrupole splitting value (1.01 mm s^{-1}). Next, in the Cu^{+}_{4c} structure of $Fe^{2+,HS}\cdots OH^{-}$-$Cu^{+}(Y237)$ in Table 4, the Cu–N(His233) and Cu–N(His283) distances are increased and the Cu–O, Cu–N(282), and Fe···Cu distances are decreased; meanwhile, the calculated $^{57}Fe^{2+}$ Mössbauer isomer shift (0.92 mm s^{-1}) is decreased, and its quadruple splitting value (1.20 mm s^{-1}) is increased. Further, the trend continues in the four $Fe^{2+,HS}\cdots OH^{-}$-$Cu^{+}_{3c/2c}(Y237)(H376H^{+})^{(1-4)}$ structures in Table 5, that is, with a decrease in the Cu^{+} coordination number and the $Fe^{2+}\cdots Cu^{+}$ distance, the calculated $^{57}Fe^{2+}$ Mössbauer isomer shift decreases and its quadrupole splitting value increases. In particular, the ΔE_Q values (1.32 and 1.51 mm s^{-1}) of $Fe^{2+,HS}\cdots OH^{-}$-$Cu^{+}_{3c}(Y237)(H376H^{+})^{(1)}$ and $Fe^{2+,HS}\cdots OH^{-}$-$Cu^{+}_{3c}(Y237)(H376H^{+})^{(2)}$ structures are very close to the observed ΔE_Q = 1.43 mm s^{-1} of the first $^{57}Fe_{a3}{}^{2+}$ Mössbauer component.[18] It is therefore probable that the DNC structure of the first (majority) $^{57}Fe_{a3}{}^{2+}$ component observed in the Mössbauer experiment is trapped at a structure similar to the ones in $Fe^{2+,HS}\cdots OH^{-}$-$Cu^{+}_{3c}(Y237)(H376H^{+})^{(1)/(2)}$ at low temperature.

It is not evident whether the His376 side chain is typically protonated or not. To see how the protonation state of His376 affects the Mössbauer properties of the $^{57}Fe^{2+}$ site, we deleted the added proton on $His376^{+}$ in $Fe^{2+,HS}\cdots OH^{-}$-$Cu^{+}_{3c/2c}(Y237)$-$(H376H^{+})^{(1-4)}$ and optimized the geometries with fixed atom positions of Fe, Cu, N(His233), N(His283), and N(His283). The calculated properties of these four partially optimized DNC structures, $Fe^{2+,HS}\cdots OH^{-}$-$Cu^{+}_{3c/2c}(Y237)^{(1-4)}$ are also given in Table 5 (rows 7–10 with footnote e). The calculated net spin populations on Fe^{2+} and Cu^{+}, and the Mössbauer isomer shifts and quadrupole splittings of the four $Fe^{2+,HS}\cdots OH^{-}$-$Cu^{+}_{3c/2c}(Y237)^{(1-4)}$ structures, are essentially the same as the corresponding ones of $Fe^{2+,HS}\cdots OH^{-}$-$Cu^{+}_{3c/2c}(Y237)$-$(H376H^{+})^{(1-4)}$. Therefore, the protonation state of the His376 side chain does not affect the Mössbauer properties of the $^{57}Fe^{2+}$ site.

The calculated pK_as of His376-H^{+} are larger than 10, which indicates that the system favors this charge neutral state. Without including the carboxylate group of the Glu126B side chain (which is within a strong H-bonding distance of $N_{\varepsilon 2}$ of the His376 side chain) in the DNC quantum cluster model, it is not clear whether the His376 side chain would be protonated in a realistic protein environment.

If we use the energies of $Fe^{2+,HS}\cdots OH^{-}$-$Cu^{+}_{2c}(Y237)$ (second row of Table 5) and $Fe^{2+,HS}\cdots H_2O$-$Cu^{+}(Y237)$ (second row of Table 4) to calculate the pK_a of the H_2O molecule, we obtain a value of 12.7. These structures differ very significantly in Cu^{+} coordination geometry. We then protonated the OH^{-} ligand in the optimized structure $Fe^{2+,HS}\cdots OH^{-}$-$Cu^{+}_{2c}(Y237)$ (see the left structure in Figure 7) and performed geometry optimization to see if the linear H_2O-Cu^{+}_{2c}-N(His282) configuration would persist. However, during the geometry optimization, the H_2O–Cu^{+} distance was gradually lengthened and the Cu^{+}–N(His233) distance shortened, and the Cu^{+} site became 3-coordinate with ligands His233, His282, and H_2O (see the middle structure in Figure 7).

The relative energy of a middle $Fe^{2+,HS}\cdots H_2O$-$Cu^{+}_{3c}(Y237)$ state (−368.9 kcal mol^{-1}) (footnote f in Table 5) is similar to that (−366.8 kcal mol^{-1}) of the $Fe^{2+,HS}\cdots H_2O$-$Cu^{+}(Y237)$ state (with three His ligands at the Cu^{+} site and a weak $Cu^{+}\cdots H_2O$

DOI: 10.1021/acs.inorgchem.5b00700
Inorg. Chem. 2015, 54, 7272–7290

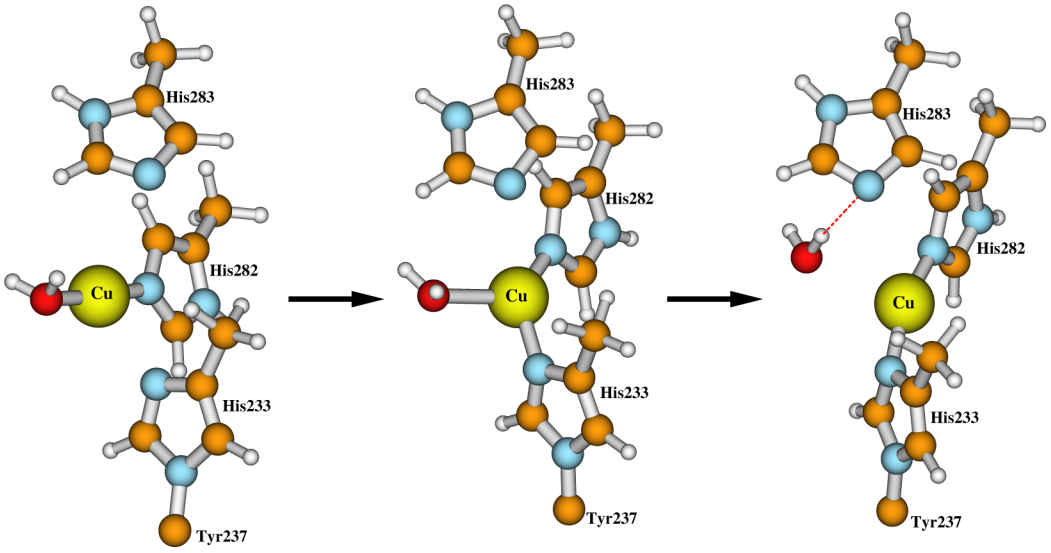

Figure 7. Changing of the Cu^{+} coordination state during the geometry optimization calculation after manually protonating the OH^{-} ligand in $Fe^{2+,HS}\cdots OH^{-}$-Cu^{+}_{2c}(Y237) (second row of Table 5). Left: The initial linear H_2O-Cu^{+}_{2c}-N(His282) structure when adding a proton to the OH^{-} ligand. Other parts of the model cluster are similar to those in Figure 5 but with a neutral His376 side chain. Middle: During the geometry optimization, the O–Cu^{+} distance lengthens, the His233 side chain rebinds with Cu^{+}, and a 3-coordinate Cu^{+} configuration is formed (see $Fe^{2+,HS}\cdots H_2O$-Cu^{+}_{3c}(Y237) with footnote f in Table 5). Right: The H_2O ligand eventually dissociates from the Cu^{+} site, and a 2-coordinate N(His233)-Cu^{+}_{2c}-N(His282) configuration is obtained (see $Fe^{2+,HS}\cdots H_2O\cdots Cu^{+}_{2c}$(Y237) in Table 5).

interaction), as given in Table 4. As the geometry optimization continued, the H_2O molecule and the Cu^{+} center continued moving away from each other, and finally the H_2O dissociated from the Cu^{+} site and H-bonded with the His283 side chain. The 2-coordinate His233-Cu^{+}_{2c}-His282 center is shown on the right side of Figure 7, and the calculated properties of this model cluster are given in the last row of Table 5. This structure has a very long Fe···Cu distance of 5.92 Å and is ∼10 kcal mol^{-1} lower in energy than the middle $Fe^{2+,HS}\cdots H_2O$-Cu^{+}_{3c}(Y237) state. We do not know if such an $Fe^{2+,HS}\cdots H_2O\cdots Cu^{+}_{2c}$(Y237) state is feasible during the catalytic cycle given other protein geometric constraints. For example, both Fe···Cu (5.92 Å) and Cu–N(H283) (5.40 Å) distances are very long. However, our calculations indeed show the mobility of the His233 and His283 side chains, which can be potential proton loading sites during the catalytic cycle and proton pumping.

We note that the calculated Mössbauer properties of both the $Fe^{2+,HS}\cdots H_2O$-Cu^{+}_{3c}(Y237) and $Fe^{2+,HS}\cdots H_2O\cdots Cu^{+}_{2c}$(Y237) states ($\delta$ = 0.91 mm s^{-1}, ΔE_Q = 2.31/2.24 mm s^{-1}) are also similar to those of the open $Fe^{2+,HS}\cdots Cu^{+}$(Y237^{-}/Y237) structures given in Table 2 and are consistent with the observed Mössbauer properties for the second $^{57}Fe_{a3}{}^{2+}$ component. Therefore, up until now, one cannot draw an exclusive conclusion about the DNC structure of the second observed $^{57}Fe_{a3}{}^{2+}$ component in the Mössbauer experiments.[18]

3.5. Fe^{2+}-$(HO_2)^{-}$-Cu^{+} DNC Models from 3S8G. In ref 23, on the basis of a series of structural calculations and comparisons, we proposed that the dioxygen species found in the DNC of 3S8G is HO_2^{-} with the majority species having the proton of the HO_2^{-} residing on the oxygen atom that is closer to the Fe^{2+} site in the Fe^{2+}-(HO-O)$^{-}$-Cu^{+} conformation. Details of the optimized 3S8G-$Fe^{2+,LS/IS/HS}$-$(HO_2)^{-}$-Cu^{+}(Y237^{-}/Y237) DNC structures are given in Tables 4–8 of ref 23. We have now performed Mössbauer property calculations on those structures. It turns out that the calculated Mössbauer properties of the 3S8G-$Fe^{2+,LS/IS/HS}$-$(HO_2)^{-}$-Cu^{+}(Y237^{-}/Y237) DNC models, which are given in Tables S1 and S2 in the Supporting Information, are not consistent with either of the observed $^{57}Fe_{a3}{}^{2+}$ Mössbauer properties. This also supports the conclusion that the HO_2^{-} species found in the 3S8G X-ray crystal structure arises from the recombination of two radiation produced HO· radicals (product of water radiolysis) formed very near or even between the two metal sites,[15] or comes from the photoreaction of the H_2O/OH^{-} between the as-isolated oxidized Fe^{3+} and Cu^{2+} sites in the X-ray beam.[23] Next, we will examine if Fe^{3+}-$OH^{-}\cdots H_2O$-Cu^{2+}- and Fe^{3+}-$H_2O\cdots OH^{-}$-Cu^{2+}-type model clusters represent the DNC structures observed in the Mössbauer experiments for the oxidized ba_3 *Cc*O from *Tt*.

4. RESULTS AND DISCUSSION ON THE Fe^{3+}/Cu^{2+} OXIDIZED STATE DNC MODEL CALCULATIONS

4.1. The Fe^{3+}-$OH^{-}\cdots H_2O$-Cu^{2+} and Fe^{3+}-$H_2O\cdots OH^{-}$-Cu^{2+} DNC Models from 3S8G. The initial model structures in this subsection are constructed by replacing the dioxygen atoms observed in the DNC of 3S8G (Figures 1 and 2 of ref 23) with the $OH^{-}\cdots H_2O/H_2O\cdots OH^{-}$ species. The central structures of the Fe^{3+}-$OH^{-}\cdots H_2O$-Cu^{2+} and Fe^{3+}-$H_2O\cdots OH^{-}$-Cu^{2+} model clusters are shown in Figures 8 and 9, respectively.

We have optimized the geometries and calculated the Mössbauer properties of the Fe^{3+}-$OH^{-}\cdots H_2O$-Cu^{2+} and Fe^{3+}-$H_2O\cdots OH^{-}$-Cu^{2+} model clusters with the Tyr237 side chain in either the deprotonated (Y237^{-}) or neutral protonated (Y237) state and with Fe^{3+} in either the LS, IS, or HS state, which is F- or AF-coupled to the Cu^{2+} site. The calculated properties are given in Tables 6 and 7, respectively, for the Fe^{3+}-$OH^{-}\cdots H_2O$-Cu^{2+} and Fe^{3+}-$H_2O\cdots OH^{-}$-Cu^{2+} model clusters.

In Table 6, we failed to obtain the optimized $Fe^{3+,IS}$-$OH^{-}\cdots H_2O$-Cu^{2+}(Y237^{-})(AF) and $Fe^{3+,HS}$-$OH^{-}\cdots H_2O$-Cu^{2+}(Y237^{-})(AF) structures, but instead, the geometry optimizations of these two states led to the lower-energy $Fe^{3+,LS}$-$OH^{-}\cdots H_2O$-Cu^{2+}(Y237^{-})(F) and $Fe^{3+,IS}$-$OH^{-}\cdots H_2O$-Cu^{2+}(Y237^{-})(F) states, respectively. The properties given for $Fe^{3+,IS}$-$OH^{-}\cdots H_2O$-Cu^{2+}(Y237^{-})(AF) and $Fe^{3+,HS}$-$OH^{-}\cdots H_2O$-Cu^{2+}(Y237^{-})-

DOI: 10.1021/acs.inorgchem.5b00700
Inorg. Chem. 2015, 54, 7272–7290

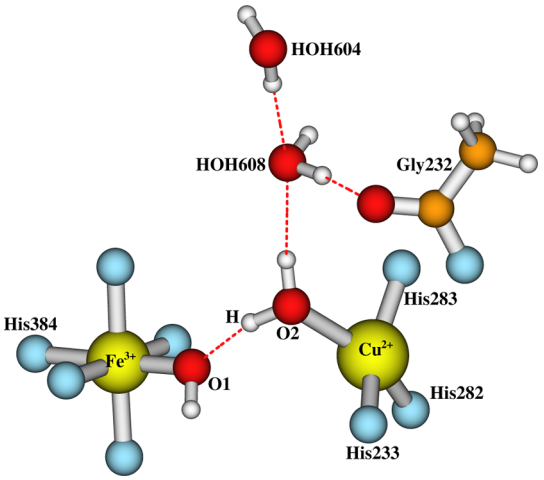

Figure 8. Detailed central portion of the Fe^{3+}-OH^{-}···H_2O-Cu^{2+} cluster generated by modifying the oxidized 3S8G DNC model. The rest of the model cluster is shown in Figures 1 and 2 of ref 23.

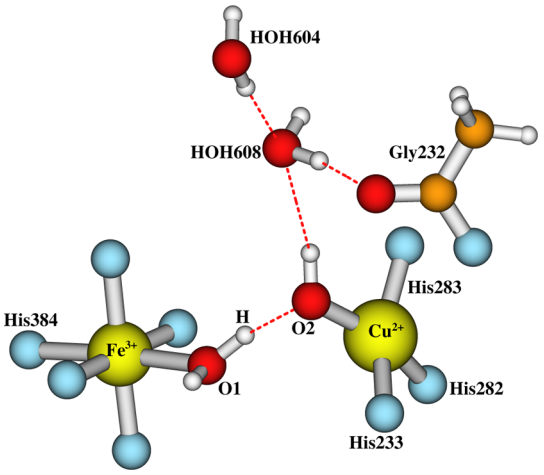

Figure 9. Detailed central portion of the Fe^{3+}-H_2O···OH^{-}-Cu^{2+} cluster generated by modifying the oxidized 3S8G DNC model. The rest of the model cluster is shown in Figures 1 and 2 of ref 23.

(AF) states were obtained from the broken-symmetry single-point energy calculations on the optimized $Fe^{3+,IS}$-OH^{-}···H_2O-$Cu^{2+}(Y237^{-})(F)$ and $Fe^{3+,HS}$-OH^{-}···H_2O-$Cu^{2+}(Y237^{-})(F)$ geometries, respectively. We did not obtain the optimized $Fe^{3+,IS}$-OH^{-}···H_2O-$Cu^{2+}(Y237)(F/AF)$ structures (neutral Tyr237) either because the proton on the Cu^{2+}-bound H_2O ligand, which originally H-bonded to the $Fe^{3+,IS}$-bound OH^{-} ligand, spontaneously transferred to the OH^{-} during the geometry optimizations, and the $Fe^{3+,IS}$-H_2O···OH^{-}-$Cu^{2+}(Y237)(F/AF)$ states were obtained.

The calculated pK_a values (3.4−5.5) in Table 6 show that the Tyr237 side chain favors the deprotonated anionic state ($Y237^{-}$) when the DNC has the Fe^{3+}-OH^{-}···H_2O-Cu^{2+}-type structure no matter whether Fe^{3+} is in LS or HS state and F- or AF-coupled with Cu^{2+}.

The $Fe^{3+,LS}$-OH^{-}···H_2O-$Cu^{2+}(Y237^{-})(F)$ and $Fe^{3+,LS}$-OH^{-}···H_2O-$Cu^{2+}(Y237^{-})(AF)$ states have very similar energies (with only 0.5 kcal mol^{-1} difference), and they are 2−3 kcal mol^{-1} and >5 kcal mol^{-1} lower in energy than the $Fe^{3+,IS}$-OH^{-}···H_2O-$Cu^{2+}(Y237^{-})(F/AF)$ and $Fe^{3+,HS}$-OH^{-}···H_2O-$Cu^{2+}(Y237^{-})(F/AF)$ states, respectively. Therefore, if the oxidized DNC has the Fe^{3+}-OH^{-}···H_2O-Cu^{2+}-type structure at 4.2 K, it is expected to be in the $Fe^{3+,LS}$-OH^{-}···H_2O-$Cu^{2+}(Y237^{-})(F/AF)$ state. The calculated ΔE_Q = 2.53/2.16 mm s^{-1} for the $Fe^{3+,LS}$-OH^{-}···H_2O-$Cu^{2+}(Y237^{-})(F/AF)$ states are in good agreement with the experimentally observed value ΔE_Q = 2.24 mm s^{-1} for the "low-spin" $^{57}Fe_{a3}{}^{3+}$ species at 4.2 K < T < 190 K.[18] The calculated δ = 0.19/0.21 mm s^{-1} of these two states are ∼0.1 mm s^{-1} smaller than, but are still reasonably consistent with, the corresponding observed value of δ = 0.29 mm s^{-1} (see Figure 1).

For the Fe^{3+}-H_2O···OH^{-}-Cu^{2+} DNC model calculations in Table 7, during geometry optimizations starting from the $Fe^{3+,LS}$-H_2O···OH^{-}-$Cu^{2+}(Y237^{-})(F/AF)$ clusters (see Figure 9), the proton on the $Fe^{3+,LS}$-bound H_2O ligand, which originally H-bonded to the Cu^{2+}-bound OH^{-} ligand, transferred to the OH^{-}. As a result, the $Fe^{3+,LS}$-OH^{-}···H_2O-$Cu^{2+}(Y237^{-})(F/AF)$ states (in Table 6 and Figure 8) were obtained. Therefore, Table 7 shows only the $Fe^{3+,IS}$-H_2O···OH^{-}-Cu^{2+} and $Fe^{3+,HS}$-H_2O···OH^{-}-Cu^{2+} state calculations; these forms are stable under geometry optimization.

The calculated pK_as of the Tyr237 side chain for the $Fe^{3+,IS}$-H_2O···OH^{-}-Cu^{2+} and $Fe^{3+,HS}$-H_2O···OH^{-}-Cu^{2+} clusters are 6.6−7.2 (Table 7). Considering the uncertainty of DFT calculations and the fact that the pK_a calculations are for the equilibrium state at room temperature, it is not certain whether the Tyr237 side chains of the $Fe^{3+,IS/HS}$-H_2O···OH^{-}-Cu^{2+}-type DNCs are in the neutral or anionic state under the Mössbauer experimental conditions. The very short O···O distance (2.66 Å) between the Tyr237 side chain and the geranyl side chain of a_3-heme in 3S8G implies that the Tyr237 is in the deprotonated anion form in this radiolyticly reduced X-ray crystal structure.[23] However, in ref 23, our calculations have shown that Tyr237 energetically favors the neutral protonated form in the reduced $Fe^{2+,LS/IS/HS}$-$(HO_2)^{-}$-Cu^{+} DNC. Therefore, Tyr237 is likely in the anionic state in the oxidized protein before the X-ray irradiation and is trapped at very low temperature after the irradiation.

The $Fe^{3+,IS}$-H_2O···OH^{-}-$Cu^{2+}(Y237^{-})(F/AF)$ states are 4.3−4.7 kcal mol^{-1} lower in energy than the $Fe^{3+,HS}$-H_2O···OH^{-}-$Cu^{2+}(Y237^{-})(F/AF)$ states (Table 7). In addition, the energies of the $Fe^{3+,IS}$-H_2O···OH^{-}-$Cu^{2+}(Y237^{-})(F/AF)$ states (Table 7) are very similar to the energies of the $Fe^{3+,LS}$-OH^{-}···H_2O-$Cu^{2+}(Y237^{-})(F/AF)$ states (Table 6). The calculated quadrupole splittings for the $Fe^{3+,IS}$-H_2O···OH^{-}-$Cu^{2+}(Y237^{-})(F/AF)$ states (2.42/2.42 mm s^{-1}) are also similar to those for the $Fe^{3+,LS}$-OH^{-}···H_2O-$Cu^{2+}(Y237^{-})(F/AF)$ states (2.53/2.16 mm s^{-1}). Further, the average (avg) of the four calculated isomer shifts and quadrupole splittings (δ^{avg} = 0.30 mm s^{-1}, $\Delta E_Q{}^{avg}$ = 2.38 mm s^{-1}) of the $Fe^{3+,IS}$-H_2O···OH^{-}-$Cu^{2+}(Y237^{-})(F/AF)$ and $Fe^{3+,LS}$-OH^{-}···H_2O-$Cu^{2+}(Y237^{-})(F/AF)$ states agrees very well with the experimentally observed spectra (δ = 0.29 mm s^{-1}, ΔE_Q = 2.24 mm s^{-1}), which was suggested as a "low-spin" $^{57}Fe_{a3}{}^{3+}$ species at 4.2 K < T < 190 K.[18] We therefore propose that this "low-spin" $^{57}Fe_{a3}{}^{3+}$ species observed in the Mössbauer experiment at 4.2 K < T < 190 K is a mixture of the $Fe^{3+,IS}$-H_2O···OH^{-}-$Cu^{2+}(Y237^{-})(F/AF)$ and $Fe^{3+,LS}$-OH^{-}···H_2O-$Cu^{2+}(Y237^{-})(F/AF)$ states.

It was reported that this "low-spin" $^{57}Fe_{a3}{}^{3+}$ component underwent a transition to a "high-spin" species with $\Delta E_Q \approx 1$ mm s^{-1} when the temperature was increased above 190 K, and the transition was complete at 245 K.[18] The isomer shift of this new "high-spin" $^{57}Fe_{a3}{}^{3+}$ species was not given in ref 18. We notice that the calculated ΔE_Q values of the $Fe^{3+,IS}$-OH^{-}···H_2O-$Cu^{2+}(Y237^{-})(F/AF)$ (in Table 6) and $Fe^{3+,HS}$-H_2O···OH^{-}-

DOI: 10.1021/acs.inorgchem.5b00700
Inorg. Chem. 2015, 54, 7272−7290

Table 6. Calculated Properties of the Oxidized Fe^{3+}-OH^-···H_2O-Cu^{2+}(Y237$^-$/Y237) Clusters Generated from the DNC of the X-ray Crystal Structure 3S8G[a]

	geometry												net spin		$^{57}Fe^{3+}$ Mössbauer	
state[b]	Fe−N (H384)	Fe−O1	Cu−O2	O1···O2	Fe···Cu	Cu−N (H233)	Cu−N (H282)	Cu−N (H283)	O···O (Y237)	E[c]	pK_a (Y237)	Q	Fe^{3+}	Cu^{2+}	δ	ΔE_Q
$Fe^{3+,LS}$-OH^-···H_2O-Cu^{2+}(Y237$^-$)(F)	2.09	1.84	2.36	2.66	5.47	2.05	2.09	2.04	3.04	−58.8		0	1.04	0.33	0.19	2.53
$Fe^{3+,LS}$-OH^-···H_2O-Cu^{2+}(Y237$^-$) (AF)	2.09	1.85	2.32	2.63	5.40	2.05	2.09	2.04	3.02	−58.3		0	0.95	−0.35	0.21	2.16
$Fe^{3+,IS}$-OH^-···H_2O-Cu^{2+}(Y237$^-$)(F)	2.43	2.00	2.20	2.51	5.31	2.07	2.09	2.06	3.08	−56.1		0	2.71	0.38	0.39	1.57
$Fe^{3+,IS}$-OH^-···H_2O-Cu^{2+}(Y237$^-$) (AF)[d]										−56.3		0	2.69	−0.38	0.39	1.64
$Fe^{3+,HS}$-OH^-···H_2O-Cu^{2+}(Y237$^-$)(F)	2.42	1.95	2.23	2.59	5.24	2.08	2.07	2.05	3.01	−51.1		0	4.10	0.38	0.36	0.21
$Fe^{3+,HS}$-OH^-···H_2O-Cu^{2+}(Y237$^-$) (AF)[e]										−53.0		0	4.10	−0.37	0.36	0.21
$Fe^{3+,LS}$-OH^-···H_2O-Cu^{2+}(Y237)(F)	2.08	1.83	2.28	2.68	5.45	2.06	2.10	2.03	3.29	−49.7	5.0	1	1.28	0.39	0.14	2.07
$Fe^{3+,LS}$-OH^-···H_2O-Cu^{2+}(Y237)(AF)	2.09	1.85	2.13	2.58	5.41	2.07	2.08	2.02	3.39	−48.1	3.4	1	0.85	−0.46	0.19	2.25
$Fe^{3+,HS}$-OH^-···H_2O-Cu^{2+}(Y237)(F)	2.38	1.99	2.05	2.48	5.26	2.07	2.05	2.02	3.42	−43.8	5.5	1	4.12	0.51	0.39	0.32
$Fe^{3+,HS}$-OH^-···H_2O-Cu^{2+}(Y237)(AF)	2.42	1.97	2.06	2.49	5.25	2.07	2.06	2.02	3.50	−45.5	5.4	1	4.10	−0.50	0.36	0.39

[a]The properties include geometries (Å), electronic energies (E, offset by −28200 kcal mol^{-1} in this table and in Table 7) obtained from the all-electron/all-TZP single-point energy calculations on the optimized geometries, pK_a's, the net charge (Q) of the clusters, Mulliken net spin polarizations for the Fe and Cu sites, and the ^{57}Fe Mössbauer isomer shifts (δ, mm s^{-1}) and quadrupole splittings (ΔE_Q, mm s^{-1}). [b]F stands for ferromagnetically coupled and AF for antiferromagnetically coupled. [c]The energies calculated for the AF-coupled states are broken-symmetry state energies. [d]A broken-symmetry single-point energy calculation on the $Fe^{3+,IS}$-OH^-···H_2O-Cu^{2+}(Y237$^-$)(F) optimized geometry. [e]A broken-symmetry single-point energy calculation on the $Fe^{3+,HS}$-OH^-···H_2O-Cu^{2+}(Y237$^-$)(F) optimized geometry.

DOI: 10.1021/acs.inorgchem.5b00700
Inorg. Chem. 2015, 54, 7272−7290

Table 7. Calculated Properties of the Oxidized Fe^{3+}-H_2O···OH^--Cu^{2+}(Y237$^-$/Y237) Clusters Generated from the DNC of the X-ray Crystal Structure 3S8G[a]

	geometry												net spin		$^{57}Fe^{3+}$ Mössbauer	
state[b]	Fe–N (H384)	Fe–O1	Cu–O2	O1···O2	Fe···Cu	Cu–N (H233)	Cu–N (H282)	Cu–N (H283)	O···O (Y237)	E^c	pK_a (Y237)	Q	Fe^{3+}	Cu^{2+}	δ	ΔE_Q
$Fe^{3+,IS}$-H_2O···OH^--Cu^{2+}(Y237$^-$)(F)	2.27	2.29	1.94	2.58	5.48	2.09	2.06	2.06	2.93	−58.7		0	2.74	0.50	0.40	2.42
$Fe^{3+,IS}$-H_2O···OH^--Cu^{2+}(Y237$^-$)(AF)	2.26	2.28	1.94	2.57	5.48	2.08	2.06	2.06	2.91	−58.4		0	2.74	−0.50	0.39	2.42
$Fe^{3+,HS}$-H_2O···OH^--Cu^{2+}(Y237$^-$)(F)	2.20	2.31	1.93	2.60	5.53	2.09	2.05	2.05	3.02	−54.1		0	4.06	0.51	0.52	1.49
$Fe^{3+,HS}$-H_2O···OH^--Cu^{2+}(Y237$^-$)(AF)	2.19	2.29	1.93	2.58	5.53	2.09	2.05	2.05	2.99	−54.0		0	4.07	−0.52	0.50	1.40
$Fe^{3+,IS}$-H_2O···OH^--Cu^{2+}(Y237)(F)	2.27	2.29	1.93	2.59	5.49	2.10	2.07	2.05	3.39	−51.9	6.6	1	2.75	0.52	0.39	2.49
$Fe^{3+,IS}$-H_2O···OH^--Cu^{2+}(Y237)(AF)	2.27	2.27	1.93	2.57	5.47	2.11	2.06	2.05	3.44	−52.3	6.9	1	2.74	−0.52	0.40	2.47
$Fe^{3+,HS}$-H_2O···OH^--Cu^{2+}(Y237)(F)	2.21	2.24	1.93	2.57	5.51	2.11	2.06	2.05	3.46	−48.8	7.0	1	4.11	0.52	0.47	0.88
$Fe^{3+,HS}$-H_2O···OH^--Cu^{2+}(Y237)(AF)[d]										−48.9	7.2	1	4.11	−0.52	0.47	0.88

[a]The properties include geometries (Å), electronic energies (E, offset by −28200 kcal mol^{-1} in this table and in Table 6) obtained from the all-electron/all-TZP single-point energy calculations on the optimized geometries, pK_a's, the net charge (Q) of the clusters, Mulliken net spin polarizations for the Fe and Cu sites, and the ^{57}Fe Mössbauer isomer shifts (δ, mm s^{-1}) and quadrupole splittings (ΔE_Q, mm s^{-1}). [b]F stands for ferromagnetically coupled and AF for antiferromagnetically coupled. [c]The energies calculated for the AF-coupled states are broken-symmetry state energies. [d]A broken-symmetry single-point energy calculation on the optimized $Fe^{3+,HS}$-H_2O···OH^--Cu^{2+}(Y237)(F) geometry.

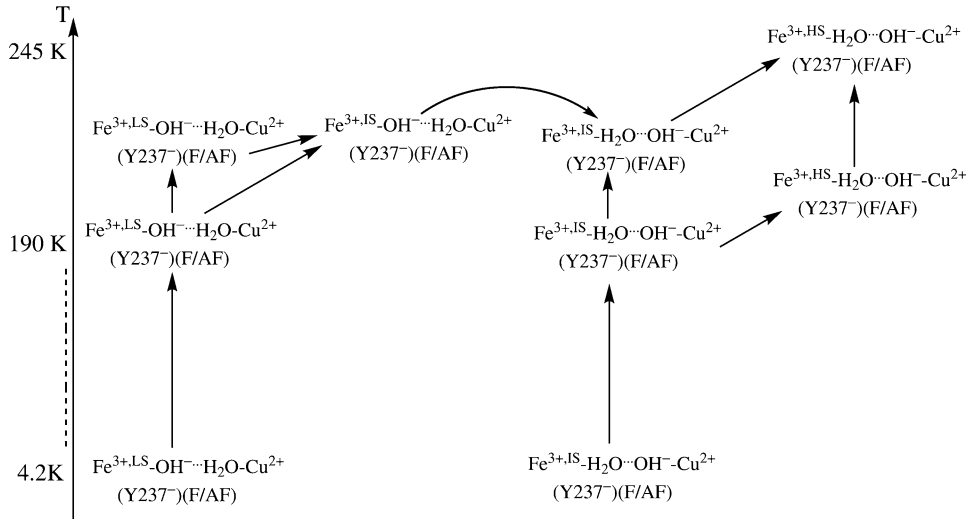

Figure 10. We propose that the so-called "low-spin" $^{57}Fe_{a3}{}^{3+}$ species observed in the Mössbauer experiments at 4.2 K < T < 190 K is a mixture of the $Fe^{3+,LS}$-OH$^-$···H_2O-Cu^{2+}(Y237$^-$)(F/AF) and $Fe^{3+,IS}$-H_2O···OH^--Cu^{2+}(Y237$^-$)(F/AF) states, which transform to the $Fe^{3+,HS}$-H_2O···OH^--Cu^{2+}(Y237$^-$)(F/AF) states with increasing temperature.

Cu^{2+}(Y237$^-$)(F/AF) (in Table 7) states are very similar (1.4–1.6 mm s^{-1}) and are close to the observed $\Delta E_Q \approx 1$ mm s^{-1}. It is likely that when the temperature is increased the $Fe^{3+,LS}$-OH$^-$···H_2O-Cu^{2+}(Y237$^-$)(F/AF) and $Fe^{3+,IS}$-H_2O···OH^--Cu^{2+}(Y237$^-$)(F/AF) states start to transform to the $Fe^{3+,IS}$-OH$^-$···H_2O-Cu^{2+}(Y237$^-$)(F/AF) and $Fe^{3+,HS}$-H_2O···OH^--Cu^{2+}(Y237$^-$)(F/AF) states, respectively. Qualitatively, one expects the vibrational entropies to increase ($\Delta S_{vib} > 0$) when $Fe^{3+,LS} \rightarrow Fe^{3+,IS}$ and $Fe^{3+,IS} \rightarrow Fe^{3+,HS}$. The vibrational entropy differences ($\Delta G_{vib} = -T\Delta S_{vib}$) are not in our current models. They require careful frequency calculations on fairly large models.

When the $Fe_{a3}{}^{3+}$ site is in the intermediate-spin state, the $Fe^{3+,IS}$-H_2O···OH^--Cu^{2+}(Y237$^-$)(F/AF) DNC clusters (in Table 7 and Figure 9) are 2–3 kcal mol^{-1} lower in energy than the $Fe^{3+,IS}$-OH$^-$···H_2O-Cu^{2+}(Y237$^-$)(F/AF) (in Table 6 and Figure 8) clusters. We have mentioned above that, during geometry optimizations of the $Fe^{3+,IS}$-OH$^-$···H_2O-Cu^{2+}(Y237)-(F/AF) structures (neutral Tyr237), the proton on the Cu^{2+}-bound H_2O ligand transferred to the Fe^{3+}-bound OH$^-$ ligand, and the $Fe^{3+,IS}$-H_2O···OH^--Cu^{2+}(Y237)(F/AF) states are obtained. Therefore, the proton transfer barrier for the transition of $Fe^{3+,IS}$-OH$^-$···H_2O-Cu^{2+}(Y237)(F/AF) → $Fe^{3+,IS}$-H_2O···OH^--Cu^{2+}(Y237)(F/AF) is small. With a further increase in temperature, the $Fe^{3+,IS}$-OH$^-$···H_2O-Cu^{2+}(Y237$^-$)-

DOI: 10.1021/acs.inorgchem.5b00700
Inorg. Chem. 2015, 54, 7272–7290

(F/AF) states (anionic tyrosine) also likely undergo proton transfer and change to the $Fe^{3+,IS}$-H_2O···OH^--Cu^{2+}($Y237^-$)(F/AF) states, which then transform to the $Fe^{3+,HS}$-H_2O···OH^--Cu^{2+}($Y237^-$)(F/AF) states. Therefore, all these transformations will end in $Fe^{3+,HS}$-H_2O···OH^--Cu^{2+}($Y237^-$)(F/AF) states at 245 K. This proposed transformation process is shown schematically in Figure 10.

To estimate the proton transfer barrier in the transformation of $Fe^{3+,IS}$-OH^-···H_2O-Cu^{2+}($Y237^-$)(F) → $Fe^{3+,IS}$-H_2O···OH^--Cu^{2+}($Y237^-$)(F) (energy difference ΔE = −2.6 kcal mol^{-1}), starting from the optimized geometry of $Fe^{3+,IS}$-OH^-···H_2O-Cu^{2+}($Y237^-$)(F), we gradually moved the proton on O2 (see Figure 8) toward the oxygen atom O1 along the H···O1 direction, then optimized the cluster with the position of this proton (labeled as H in Figure 8) fixed. The electronic energies of these optimized clusters with different fixed-H positions are very similar to the originally optimized $Fe^{3+,IS}$-OH^-···H_2O-Cu^{2+}($Y237^-$)(F) cluster. The highest energy structure we obtained is only 2.0 kcal mol^{-1} higher than the energy of the lowest-energy $Fe^{3+,IS}$-OH^-···H_2O-Cu^{2+}($Y237^-$)(F) structure. The central portion of this highest-energy structure is shown in Figure 11 in which the proton H is at equal distance (1.20 Å)

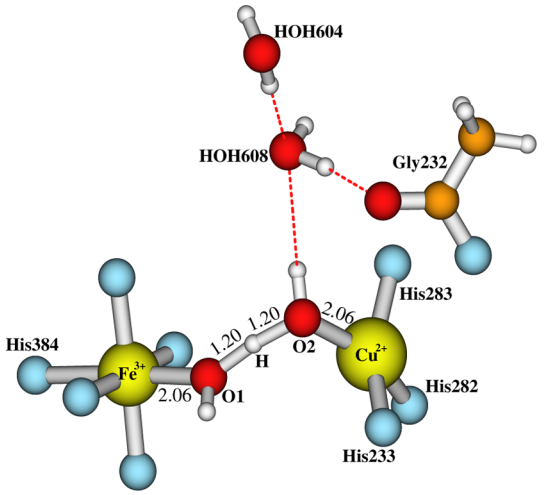

Figure 11. To estimate the energy barrier of the proton (H) transfer of $Fe^{3+,IS}$-OH^-···H_2O-Cu^{2+}($Y237^-$)(F) → $Fe^{3+,IS}$-H_2O···OH^--Cu^{2+}($Y237^-$)(F) from the position shown in Figure 8 to the position in Figure 9, we gradually moved the proton along the H···O1 direction toward the O1 atom and then optimized the cluster with the fixed position of this proton. This figure shows the detailed central portion of the highest-energy DNC structure obtained among these H-fixed optimized clusters.

with O1 and O2. The distances of Fe−O1 and Cu−O2 are also the same (2.06 Å). Because of the size of the system, we did not perform transition state search and frequency calculations. According to the features of this structure, it is reasonable to assume that it is close to the transition state of the proton transfer. Then, the barrier for this proton transfer should also be ∼2 kcal mol^{-1}, which is smaller than the energy differences (3.3/5.0 kcal mol^{-1}) between the $Fe^{3+,IS}$-OH^-···H_2O-Cu^{2+}($Y237^-$)(F/AF) and $Fe^{3+,HS}$-OH^-···H_2O-Cu^{2+}($Y237^-$)(F/AF) states (Table 6). Therefore, the $Fe^{3+,IS}$-OH^-···H_2O-Cu^{2+}($Y237^-$)(F/AF) states will transform more easily to the $Fe^{3+,IS}$-H_2O···OH^--Cu^{2+}($Y237^-$)(F/AF) states than to the $Fe^{3+,HS}$-OH^-···H_2O-Cu^{2+}($Y237^-$)(F/AF) states with increasing temperature. Such a proton transfer from the water molecule ligating the Cu^{2+} ion to the hydroxyl ligand of Fe^{3+} was also obtained in DFT calculations on the oxidized states from two aa_3 *Cc*O DNCs (bacterial, *Paracoccus denitrificans*; and mammalian, bovine) by Sharma et al.[57]

In addition, a high-spin $^{57}Fe_{a3}{}^{3+}$ species with (δ = 0.41 mm s^{-1}, ΔE_Q = 0.7 mm s^{-1}, see Figure 1) was also observed in the Mössbauer experiments on *Tt*, which did not change through the temperature range from 4.2 to 245 K.[18] Next, we present our studies on DNC models generated from the X-ray crystal structures 3EH4 and 1EHK to see if this high-spin $^{57}Fe_{a3}{}^{3+}$ species could be represented by the DNC structure containing a Cu^{2+}-terminally bound OH^- or bridging OH^- between Fe^{3+} and Cu^{2+}.

4.2. Fe^{3+}···OH^--Cu^{2+} DNC Models from 3EH4. Our calculations in sections 3.3 and 3.4 imply that the $Fe^{2+,HS}$···OH^--Cu^+ DNC in 3EH4 is probably trapped from the earlier oxidized $Fe^{3+,HS}$···OH^--Cu^{2+} (or $Fe^{3+,HS}$-H_2O···OH^--Cu^{2+}) structure after X-ray irradiation. We now geometry optimize the $Fe^{3+,HS}$···OH^--Cu^{2+}($Y237^-$/Y237)(F/AF) clusters. However, the calculations for the $Fe^{3+,HS}$···OH^--Cu^{2+}($Y237^-$/Y237)(AF) states lead instead to $Fe^{3+,IS}$···OH^--Cu^{2+}($Y237^-$/Y237)(F) states. Therefore, we present the calculated properties of both $Fe^{3+,IS/HS}$···OH^--Cu^{2+}($Y237^-$/Y237)(F) states in Table 8. In these models (and all the Fe^{3+}···Cu^{2+} DNC models in the current paper), the three histidine ligands of Cu^{2+} bind strongly with typical Cu^{2+}−N(His) distances of 2.02−2.15 Å.

The calculated pK_a values for the Tyr237 side chain show that the $Fe^{3+,IS/HS}$···OH^--Cu^{2+}($Y237^-$)(F) states with deprotonated anionic $Tyr237^-$ are energetically more stable than the corresponding $Fe^{3+,IS/HS}$···OH^--Cu^{2+}(Y237)(F) states. Further, the $Fe^{3+,IS}$···OH^--Cu^{2+}($Y237^-$)(F) state is 2.3 kcal mol^{-1} lower in energy than the $Fe^{3+,HS}$···OH^--Cu^{2+}($Y237^-$)(F) state. Therefore, if the Fe^{3+}···OH^--Cu^{2+}($Y237^-$)-type DNC exists, it will be in the $Fe^{3+,IS}$···OH^--Cu^{2+}($Y237^-$) state at low temperature and will likely transform to the $Fe^{3+,HS}$···OH^--Cu^{2+}($Y237^-$) state as the temperature increases, a feature similar to the $Fe^{3+,IS}$-H_2O···OH^--Cu^{2+}($Y237^-$) → $Fe^{3+,HS}$-H_2O···OH^--Cu^{2+}($Y237^-$) transition proposed in the previous section. The calculated Mössbauer properties (δ = 0.41/0.57 mm s^{-1}, ΔE_Q = 2.38/1.93 mm s^{-1}) of the $Fe^{3+,IS/HS}$···OH^--Cu^{2+}($Y237^-$)(F) states are also fairly similar to the corresponding properties (δ = 0.40/0.52 mm s^{-1}, ΔE_Q = 2.42/1.49 mm s^{-1}) of the $Fe^{3+,IS/HS}$-H_2O···OH^--Cu^{2+}($Y237^-$)(F) states. Therefore, the $Fe^{3+,HS}$···OH^--Cu^{2+}($Y237^-$) DNC model does not represent the high-spin $^{57}Fe_{a3}{}^{3+}$ species observed with δ = 0.41 mm s^{-1} and ΔE_Q = 0.7 mm s^{-1} through 4.2−245 K in the Mössbauer experiments.[18]

4.3. Fe^{3+}-OH^--Cu^{2+} DNC Models from 1EHK. The 1EHK-Fe^{3+}-OH-Cu^{2+} DNC model shown in Figure 2 was geometry optimized with Fe^{3+} in LS, IS, and HS states F- or AF-coupled with the Cu^{2+} site and with Tyr237 side chain in neutral or an anionic state. The main calculated properties of these 1EHK-Fe^{3+}-OH-Cu^{2+} cluster models are given in Table 9. Note that we did not obtain the optimized structures for the $Fe^{3+,LS}$-OH^--Cu^{2+}($Y237^-$)(F) and $Fe^{3+,IS}$-OH^--Cu^{2+}($Y237^-$)(F) states. Calculations for these two states led to the $Fe^{3+,IS}$-OH^--Cu^{2+}($Y237^-$)(AF) and $Fe^{3+,HS}$-OH^--Cu^{2+}($Y237^-$)(AF) states, respectively.

The calculated pK_a(Y237) values (−0.4 and 0.6) for the $Fe^{3+,HS}$-OH^--Cu^{2+}(Y237)(F/AF) models clearly show that the $Fe^{3+,HS}$-OH^--Cu^{2+}-type DNC energetically favors the anionic form of the Tyr237 side chain.

DOI: 10.1021/acs.inorgchem.5b00700
Inorg. Chem. 2015, 54, 7272−7290

Table 8. Calculated Properties of the Oxidized $Fe^{3+}\cdots OH^{-}$-Cu^{2+}(Y237^{-}/Y237) Models Generated from the DNC of the X-ray Crystal Structure 3EH4[a]

	geometry										net spin		$^{57}Fe^{3+}$ Mössbauer	
state[b]	Fe−N	Fe···O	Cu−O	Fe···Cu	Cu−N (H233)	Cu−N (H282)	Cu−N (H283)	E	pK_a (Y237)	Q	Fe^{3+}	Cu^{2+}	δ	ΔE_Q
$Fe^{3+,IS}\cdots OH^{-}$-Cu^{2+}(Y237^{-})(F)	2.22	4.08	1.91	5.13	2.08	2.07	2.06	−165.4		0	2.62	0.52	0.41	2.38
$Fe^{3+,HS}\cdots OH^{-}$-Cu^{2+}(Y237^{-})(F)	2.10	4.29	1.91	5.32	2.08	2.07	2.06	−163.1		0	4.02	0.53	0.57	1.93
$Fe^{3+,IS}\cdots OH^{-}$-Cu^{2+}(Y237)(F)	2.19	4.11	1.91	5.18	2.11	2.07	2.05	−158.8	6.1	1	2.72	0.53	0.39	2.47
$Fe^{3+,HS}\cdots OH^{-}$-Cu^{2+}(Y237)(F)	2.08	4.25	1.91	5.33	2.11	2.07	2.05	−155.1	5.0	1	4.11	0.53	0.49	0.34

[a]The properties include geometries (Å), electronic energies (E, offset by −25100 kcal mol^{-1}) obtained from the all-electron/all-TZP single-point energy calculations on the optimized geometries, pK_a's, the net charge (Q) of the clusters, Mulliken net spin polarizations for the Fe and Cu sites, and the ^{57}Fe Mössbauer isomer shifts (δ, mm s^{-1}) and quadrupole splittings (ΔE_Q, mm s^{-1}). [b]F stands for ferromagnetically coupled.

Table 9. Calculated Properties of the Oxidized Fe^{3+}-OH^{-}-Cu^{2+}(Y237^{-}/Y237) Clusters Generated from the DNC of the 1EHK X-ray Crystal Structure[a]

	geometry											net spin		$^{57}Fe^{3+}$ Mössbauer	
state[b]	Fe−N (H384)	Fe−O	Cu−O	Fe···Cu	Cu−N (H233)	Cu−N (H282)	Cu−N (H283)	O···O (Y237)	E^c	pK_a (Y237)	Q	Fe^{3+}	Cu^{2+}	δ	ΔE_Q
$Fe^{3+,LS}$-OH^{-}-Cu^{2+}(Y237^{-})(AF)	3.72	1.81	2.72	4.31	2.02	2.08	2.04	2.80	−157.3		0	0.99	−0.29	0.24	3.03
$Fe^{3+,IS}$-OH^{-}-Cu^{2+}(Y237^{-})(AF)	3.78	1.98	2.15	3.93	2.06	2.11	2.15	2.77	−163.0		0	2.65	−0.32	0.37	2.02
$Fe^{3+,HS}$-OH^{-}-Cu^{2+}(Y237^{-})(F)	4.05	1.91	2.31	3.97	2.05	2.09	2.09	2.83	−166.1		0	4.09	0.34	0.39	0.54
$Fe^{3+,HS}$-OH^{-}-Cu^{2+}(Y237^{-})(AF)	4.08	1.91	2.30	3.97	2.05	2.10	2.09	2.82	−167.5		0	4.08	−0.29	0.38	0.51
$Fe^{3+,HS}$-OH^{-}-Cu^{2+}(Y237)(F)	4.13	1.94	2.19	3.90	2.05	2.06	2.04	3.08	−150.6	−0.4	1	4.09	0.49	0.41	0.42
$Fe^{3+,HS}$-OH^{-}-Cu^{2+}(Y237)(AF)	4.11	1.93	2.21	3.91	2.05	2.07	2.05	3.05	−153.4	0.6	1	4.04	−0.43	0.39	0.40

[a]The properties include geometries (Å), electronic energies (E, offset by −25100 kcal mol^{-1}) obtained from the all-electron/all-TZP single-point energy calculations on the optimized geometries, pK_a's, the net charge (Q) of the clusters, Mulliken net spin polarizations for the Fe and Cu sites, and the ^{57}Fe Mössbauer isomer shifts (δ, mm s^{-1}) and quadrupole splittings (ΔE_Q, mm s^{-1}). [b]F stands for ferromagnetically-coupled and AF for antiferromagnetically-coupled. [c]The energies calculated for the AF-coupled states are broken-symmetry state energies.

Both $Fe^{3+,HS}$-OH^{-}-Cu^{2+}(Y237^{-})(F) and $Fe^{3+,HS}$-OH^{-}-Cu^{2+}(Y237^{-})(AF) states yield very similar geometric and Mössbauer properties. The $Fe^{3+,HS}$-OH^{-}-Cu^{2+}(Y237^{-})(AF) state yields the lowest energy, which is 10.2, 4.5, and 1.4 kcal mol^{-1} lower in energy than the $Fe^{3+,LS}$-OH^{-}-Cu^{2+}(Y237^{-})(AF), $Fe^{3+,IS}$-OH^{-}-Cu^{2+}(Y237^{-})(AF), and $Fe^{3+,HS}$-OH^{-}-Cu^{2+}(Y237^{-})(F) states, respectively. Therefore, if the oxidized DNC exists in the Fe^{3+}-OH^{-}-Cu^{2+} form with a bridging hydroxo, it would stay in the $Fe^{3+,HS}$-OH^{-}-Cu^{2+}(Y237^{-})(AF) state. Further, we noticed that the calculated Mössbauer properties (δ = 0.38 mm s^{-1}, ΔE_Q = 0.51 mm s^{-1}) of this $Fe^{3+,HS}$-OH^{-}-Cu^{2+}(Y237^{-})(AF) state are in very good agreement with the observed Mössbauer spectra (δ = 0.41 mm s^{-1}, ΔE_Q = 0.7 mm s^{-1}).[18] Therefore, it is very likely that the $Fe^{3+,HS}$-OH^{-}-Cu^{2+}(Y237^{-})(AF) DNC structure represents the observed (δ = 0.41 mm s^{-1}, ΔE_Q = 0.7 mm s^{-1}) $^{57}Fe_{a3}^{3+}$ high-spin species, which exists through the 4.2−245 K range in the the Mössbauer experiments.[18]

5. CONCLUSIONS

The X-ray crystal structures (PDB entries: 1EHK,[10] 1XME,[11] 3EH3,[12] 3EH4,[12] 3EH5,[12] 3S8F,[15] and 3S8G[15]) of the reduced ba_3 cytochrome c oxidase (CcO) from *Thermus thermophilus* (*Tt*) showed different $Fe_{a3}^{2+}\cdots Cu_B^{+}$ dinuclear center (DNC) structures. Mössbauer experiments on the ba_3 CcO from *Tt* also revealed DNC structural heterogeneities in both oxidized and reduced states. Both radiolytic reduction and chemical reduction[10−12,15] with dithionite[58] will typically generate high-energy reduced state intermediates compared to the physiological donor cytochrome c, which has a midpoint redox potential of approximately +0.20 to +0.25 V relative to SHE. By contrast, the dithionite midpoint potential is quite negative and depends also on the dithionite initial (and final) concentrations. Use of the dithionite chemical reduction data from Zimmermann et al.,[18] and from Liu et al.[12] in combination with Mayhew's[58] analysis, yields estimated dithionite midpoint potentials of about −0.50 and −0.45 V, respectively. So there is an additional reductive driving force of about 0.7 to 0.8 V using dithionite relative to cytochrome c. Radiolytic reduction of the X-ray structures in the synchrotron X-ray beam is also highly reducing[10−12,15] although less predictable. The resulting unstable or metastable intermediates can be trapped at low temperatures (the Cryogenic X-ray structures are at ∼100 K). The X-ray structures in Table 1 (particularly 3EH3 and 3EH5) are consistent with the view that chemical reduction prior to freezing in liquid N_2 and X-ray irradiation yield more geometrically and energetically relaxed structures.

DOI: 10.1021/acs.inorgchem.5b00700
Inorg. Chem. 2015, 54, 7272−7290

Using DFT OLYP potential, we have performed geometric, energetic, and Mössbauer property calculations on the DNCs of the X-ray crystal structures listed above. Our calculations support that the $^{57}Fe_{a3}{}^{2+}$ sites observed in the Mössbauer experiments are in high-spin states. The oxygen species between the Fe^{2+} and Cu^{+} sites found in 1EHK,[10] 1XME,[11] and 3EH4,[12] is better represented by a hydroxide anion (OH^{-}). The first (majority) $^{57}Fe_{a3}{}^{2+}$ component observed in the Mössbauer experiment is best represented by the DNC in the $Fe^{2+,HS}\cdots OH^{-}$-Cu^{+} state, where OH^{-} terminally binds with Cu^{+} and the Cu^{+} is in a 4- or 3-coordinate configuration. With OH^{-} as a ligand, the Cu^{+} site energetically favors a linear OH^{-}-Cu^{+}-N(His282) 2-coordinate (2c) configuration with the His233 and His283 side chains dissociating from the Cu^{+} site. However, steric interactions, especially from the side chain of Trp229 (not included in the current model calculations), which is beside the His283 side chain, the potential energy barriers for geometry rearrangement, and the low temperature under the experimental conditions may prevent the formation of the $Fe^{2+,HS}\cdots OH^{-}$-$Cu^{+}{}_{2c}$ state. Further, a reduced DNC with OH^{-} between the $Fe^{2+,HS}$ and the Cu^{+} sites are not in the equilibrium state. The system strongly favors a water molecule (if there is solvent oxygen species) rather than a hydroxide anion in the DNC. Therefore, the reduced $Fe^{2+,HS}\cdots OH^{-}$-Cu^{+}/$Fe^{2+,HS}$-OH^{-}-Cu^{+} DNCs found in the Mössbauer experiments/X-ray crystal structures should arise from the earlier oxidized state with structures like $Fe^{3+,HS}\cdots OH^{-}$-Cu^{2+}/$Fe^{3+,HS}$-OH^{-}-Cu^{2+} and be trapped at very low temperature.

Our calculations indeed have shown that the DNC structure of $Fe^{3+,HS}$-OH^{-}-Cu^{2+}(Y237^{-})(AF), in which a hydroxo bridges the AF-coupled high-spin Fe^{3+} and Cu^{2+} sites, yields very similar Mössbauer properties (δ = 0.38 mm s^{-1}, ΔE_Q = 0.51 mm s^{-1}) to the observed $^{57}Fe_{a3}{}^{3+}$ high-spin species (δ = 0.41 mm s^{-1}, ΔE_Q = 0.7 mm s^{-1}) in the temperature range of 4.2–245 K. We have also found that the DNC structure of the observed "low-spin" $^{57}Fe_{a3}{}^{3+}$ species at 4.2–190 K with (δ = 0.29 mm s^{-1}, ΔE_Q = 2.24 mm s^{-1})[18] is likely a mixture of both the $Fe^{3+,LS}$-$OH^{-}\cdots H_2O$-Cu^{2+}(Y237^{-})(F/AF) and $Fe^{3+,IS}$-$H_2O\cdots OH^{-}$-Cu^{2+}(Y237^{-})(F/AF) states, and they gradually transition to the $Fe^{3+,HS}$-$H_2O\cdots OH^{-}$-Cu^{2+}(Y237^{-})(F/AF) states with increasing temperature (see Figure 10), which explains the observed transition of "low-spin" $^{57}Fe_{a3}{}^{3+}$ to high-spin $^{57}Fe_{a3}{}^{3+}$ in the Mössbauer experiment when the temperature was increased from 190 to 245 K.[18]

Previous resonance Raman experiments on ba_3 C*c*O from *Tt* (at ambient temperature) also discovered two high-spin $Fe_{a3}{}^{3+}$ species with one in an in-plane (6-coordinated) and another in an out-of-plane (5-coordinated) configuration.[59] The high-spin $Fe_{a3}{}^{3+}$ DNCs we have proposed here, $Fe^{3+,HS}$-$H_2O\cdots OH^{-}$-Cu^{2+}(Y237^{-})(F/AF) and $Fe^{3+,HS}$-OH^{-}-Cu^{2+}(Y237^{-})(AF), are indeed in 6- and 5- coordinated configurations, respectively. The average dihedral angle between Fe^{3+} and three of the four ligating interior N atoms in the $Fe^{3+,HS}$-$H_2O\cdots OH^{-}$-Cu^{2+}(Y237^{-})(F/AF) structures is 5°, whereas the corresponding value in $Fe^{3+,HS}$-OH^{-}-Cu^{2+}(Y237^{-})(AF) is −20°. The Fe^{3+} ion in the $Fe^{3+,HS}$-OH^{-}-Cu^{2+}(Y237^{-})(AF) structure is certainly in the out-of-plane position toward the bridging OH^{-}.

Very recently, Sharma et al. presented their computational study of a metastable but activated ferric/cupric state (O_H in their notation) in the catalytic cycle of aa_3 C*c*O.[57] The experimental evidence suggests that the DNC in the catalytically relevant O_H state may have high-spin $Fe_{a3}{}^{3+}$ with a strongly H-bonded distal hydroxide ligand and $Cu_B{}^{2+}$ with a raised redox potential.[57] On the basis of their DFT calculations, Sharma et al. have proposed that the high energy and high redox potential of Cu_B in the O_H state may stem from a 3-coordinated near-planar geometry of $Cu_B{}^{2+}$ (first alternative).[57] As a second alternative, they have also proposed that the DNC may be compact in state O_H with a very short Fe–Cu distance and a bridging μ-hydroxo between the two metals.[57] Note that this proposed second alternative O_H structure has a very similar DNC structure to our calculated $Fe^{3+,HS}$-OH^{-}-Cu^{2+}(Y237^{-})-(AF) state.

To date, several DNC structures in our calculations yield very similar $^{57}Fe^{2+,HS}$ Mössbauer properties, which are very close to the properties of the second $^{57}Fe_{a3}{}^{2+}$ component observed in the Mössbauer experiments (Figure 1).[18] These structures include: (**1**) the open $Fe^{2+,HS}\cdots Cu^{+}$ DNC structure as observed in the X-ray crystal structures 3EH3 and 3EH5,[12] where no oxygen species is between the $Fe^{2+,HS}$ and Cu^{+} sites, and the Cu^{+} binds with all three His233, His282, and His283 side chains; (**2**) similar structures to the open $Fe^{2+,HS}\cdots Cu^{+}$ structure, but with one (or more) water molecule(s) staying between but not binding with the $Fe^{2+,HS}$ and Cu^{+} sites; (**3**) the $Fe^{2+,HS}\cdots OH^{-}$-$Cu^{+}{}_{2c}$-His282 DNC structure, where the His233 and His283 side chains dissociate from Cu^{+} and the 2-coordinate Cu^{+} site linearly binds with OH^{-} and the His282 side chain; (**4**) the $Fe^{2+,HS}\cdots H_2O$-$Cu^{+}{}_{3c}$-type structure, in which the 3-coordinate Cu^{+} site binds with an H_2O and the His233 and His282 side chains; and (**5**) the $Fe^{2+,HS}\cdots$His233-$Cu^{+}{}_{2c}$-His282 structure with the H_2O ligand in structure (**4**) dissociating from the Cu^{+} site and the Cu^{+} binding with only the His233 and His282 side chains.

It is not known if the low coordination $Cu^{+}{}_{2c}$ state exists in the ba_3 C*c*O from *Tt* during its catalytic cycle. However, the variation of the Cu^{+} coordination state and the mobility of the His233 and His283 side chains shown in our calculations do suggest that the His233 and His283 side chains can be potential proton loading sites during the catalytic cycle and in the proton pumping process. Considering the high optimal growth temperature of *Thermus thermophilus*, such variation of the Cu^{+} coordination state is possible. If His283 side chain dissociates and is then protonated to form a $His283^{+}$ cation, the nearby Trp229 side chain could potentially stabilize this state through a cation-π interaction,[60] but the relative His283-Trp229 geometry must then be nearly optimal. Further calculations with larger DNC models, including the Trp229 side chain, are planned in the near future.

■ ASSOCIATED CONTENT

Ⓢ Supporting Information

Some additional figures, the detailed Mössbauer property calculations described in section 3.5 (Fe^{2+}-$(HO_2)^{-}$-Cu^{+} DNC Models from 3S8G), and the Cartesian coordinates for some representative OLYP-optimized clusters discussed in Tables 2–9. The Supporting Information is available free of charge on the ACS Publications website at DOI: 10.1021/acs.inorgchem.5b00700.

■ AUTHOR INFORMATION

Corresponding Author

*E-mail: lou@scripps.edu. Tel: (858) 784-2840.

Notes

The authors declare no competing financial interest.

DOI: 10.1021/acs.inorgchem.5b00700
Inorg. Chem. 2015, 54, 7272–7290

■ ACKNOWLEDGMENTS

We thank C. D. Stout for valuable discussions. We are indebted to the late Prof. J. A. Fee who contributed to both the X-ray structural and Mössbauer experimental studies, as well as to earlier DFT work, that are the essential framework for our research. We thank The Scripps Research Institute for computational resources and NIH for financial support (R01 GM100934).

■ REFERENCES

(1) Wikström, M. *Biochim. Biophys. Acta, Bioenerg.* **2012**, *1817*, 468−475.
(2) Kaila, V. R. I.; Verkhovsky, M. I.; Wikström, M. *Chem. Rev.* **2010**, *110*, 7062−7081.
(3) Konstantinov, A. A. *FEBS Lett.* **2012**, *586*, 630−639.
(4) von Ballmoos, C.; Adelroth, P.; Gennis, R. B.; Brzezinski, P. *Biochim. Biophys. Acta, Bioenerg.* **2012**, *1817*, 650−657.
(5) Iwata, S.; Ostermeier, C.; Ludwig, B.; Michel, H. *Nature* **1995**, *376*, 660−669.
(6) Qin, L.; Hiser, C.; Mulichak, A.; Garavito, R. M.; Ferguson-Miller, S. *Proc. Natl. Acad. Sci. U. S. A.* **2006**, *103*, 16117−16122.
(7) Ostermeier, C.; Harrenga, A.; Ermler, U.; Michel, H. *Proc. Natl. Acad. Sci. U. S. A.* **1997**, *94*, 10547−10553.
(8) Tsukihara, T.; Aoyama, H.; Yamashita, E.; Tomizaki, T.; Yamaguchi, H.; ShinzawaItoh, K.; Nakashima, R.; Yaono, R.; Yoshikawa, S. *Science* **1996**, *272*, 1136−1144.
(9) Svensson-Ek, M.; Abramson, J.; Larsson, G.; Tornroth, S.; Brzezinski, P.; Iwata, S. *J. Mol. Biol.* **2002**, *321*, 329−339.
(10) Soulimane, T.; Buse, G.; Bourenkov, G. P.; Bartunik, H. D.; Huber, R.; Than, M. E. *EMBO J.* **2000**, *19*, 1766−1776.
(11) Hunsicker-Wang, L. M.; Pacoma, R. L.; Chen, Y.; Fee, J. A.; Stout, C. D. *Acta Crystallogr., Sect. D: Biol. Crystallogr.* **2005**, *61*, 340−343.
(12) Liu, B.; Chen, Y.; Doukov, T.; Soltis, S. M.; Stout, C. D.; Fee, J. A. *Biochemistry* **2009**, *48*, 820−826.
(13) Aoyama, H.; Muramoto, K.; Shinzawa-Itoh, K.; Hirata, K.; Yamashita, E.; Tsukihara, T.; Ogura, T.; Yoshikawa, S. *Proc. Natl. Acad. Sci. U. S. A.* **2009**, *106*, 2165−2169.
(14) Koepke, J.; Olkhova, E.; Angerer, H.; Muller, H.; Peng, G. H.; Michel, H. *Biochim. Biophys. Acta, Bioenerg.* **2009**, *1787*, 635−645.
(15) Tiefenbrunn, T.; Liu, W.; Chen, Y.; Katritch, V.; Stout, C. D.; Fee, J. A.; Cherezov, V. *PLoS One* **2011**, *6*, e22348.
(16) Farver, O.; Chen, Y.; Fee, J. A.; Pecht, I. *FEBS Lett.* **2006**, *580*, 3417−3421.
(17) Fee, J. A.; Case, D. A.; Noodleman, L. *J. Am. Chem. Soc.* **2008**, *130*, 15002−15021.
(18) Zimmermann, B. H.; Nitsche, C. I.; Fee, J. A.; Rusnak, F.; Munck, E. *Proc. Natl. Acad. Sci. U. S. A.* **1988**, *85*, 5779−5783.
(19) Yoshikawa, S.; Shinzawa-Itoh, K.; Nakashima, R.; Yaono, R.; Yamashita, E.; Inoue, N.; Yao, M.; Fei, M. J.; Libeu, C. P.; Mizushima, T.; Yamaguchi, H.; Tomizaki, T.; Tsukihara, T. *Science* **1998**, *280*, 1723−1729.
(20) Sakaguchi, M.; Shinzawa-Itoh, K.; Yoshikawa, S.; Ogura, T. *J. Bioenerg. Biomembr.* **2010**, *42*, 241−243.
(21) Kaila, V. R. I.; Oksanen, E.; Goldman, A.; Bloch, D. A.; Verkhovsky, M. I.; Sundholm, D.; Wikström, M. *Biochim. Biophys. Acta, Bioenerg.* **2011**, *1807*, 769−778.
(22) Fann, Y. C.; Ahmed, I.; Blackburn, N. J.; Boswell, J. S.; Verkhovskaya, M. L.; Hoffman, B. M.; Wikstrom, M. *Biochemistry* **1995**, *34*, 10245−10255.
(23) Han Du, W.-G.; Noodleman, L. *Inorg. Chem.* **2013**, *52*, 14072−14088.
(24) Handy, N. C.; Cohen, A. J. *Mol. Phys.* **2001**, *99*, 403−412.
(25) Lee, C. T.; Yang, W. T.; Parr, R. G. *Phys. Rev. B: Condens. Matter Mater. Phys.* **1988**, *37*, 785−789.
(26) Vancoillie, S.; Zhao, H. L.; Radon, M.; Pierloot, K. *J. Chem. Theory Comput.* **2010**, *6*, 576−582.
(27) Radoń, M.; Pierloot, K. *J. Phys. Chem. A* **2008**, *112*, 11824−11832.
(28) *Amsterdam Density Functional (ADF) Software*, SCM, Theoretical Chemistry, Vrije Universiteit: Amsterdam, The Netherlands. http://www.scm.com.
(29) te Velde, G.; Bickelhaupt, F. M.; Baerends, E. J.; Guerra, C. F.; Van Gisbergen, S. J. A.; Snijders, J. G.; Ziegler, T. *J. Comput. Chem.* **2001**, *22*, 931−967.
(30) Guerra, C. F.; Visser, O.; Snijders, J. G.; te Velde, G.; Baerends, E. J. Parallelisation of the Amsterdam Density Functional Program. In *Methods and techniques for computational chemistry*; Clementi, E., Corongiu, C., Eds.; STEF: Cagliari, 1995; pp 303−395.
(31) Klamt, A.; Schüürmann, G. *J. Chem. Soc., Perkin Trans. 2* **1993**, 799−805.
(32) Klamt, A. *J. Phys. Chem.* **1995**, *99*, 2224−2235.
(33) Klamt, A.; Jonas, V. *J. Chem. Phys.* **1996**, *105*, 9972−9981.
(34) Pye, C. C.; Ziegler, T. *Theor. Chem. Acc.* **1999**, *101*, 396−408.
(35) Han, W.-G.; Sandala, G. M.; Giammona, D. A.; Bashford, D.; Noodleman, L. *Dalton Trans.* **2011**, *40*, 11164−11175.
(36) Han, W.-G.; Noodleman, L. *Inorg. Chem.* **2011**, *50*, 2302−2320.
(37) Han, W.-G.; Noodleman, L. *Theor. Chem. Acc.* **2010**, *125*, 305−317.
(38) Han, W.-G.; Giammona, D. A.; Bashford, D.; Noodleman, L. *Inorg. Chem.* **2010**, *49*, 7266−7281.
(39) Han, W.-G.; Noodleman, L. *Dalton Trans.* **2009**, 6045−6057.
(40) Han, W.-G.; Noodleman, L. *Inorg. Chim. Acta* **2008**, *361*, 973−986.
(41) Han, W. G.; Liu, T. Q.; Lovell, T.; Noodleman, L. *J. Am. Chem. Soc.* **2005**, *127*, 15778−15790.
(42) Noodleman, L.; Han Du, W.-G.; Fee, J. A.; Götz, A. W.; Walker, R. C. *Inorg. Chem.* **2014**, *53*, 6458−6472.
(43) Noodleman, L. *J. Chem. Phys.* **1981**, *74*, 5737−5743.
(44) Noodleman, L.; Case, D. A. *Adv. Inorg. Chem.* **1992**, *38*, 423−470.
(45) Noodleman, L.; Lovell, T.; Han, W.-G.; Liu, T.; Torres, R. A.; Himo, F. Density Functional Theory. In *Comprehensive Coordination Chemistry II, From Biology to Nanotechnology*; Lever, A. B., Ed.; Elsevier Ltd, 2003; Vol. *2*, pp 491−510.
(46) Han, W.-G.; Liu, T.; Lovell, T.; Noodleman, L. *J. Comput. Chem.* **2006**, *27*, 1292−1306.
(47) Liu, T.; Lovell, T.; Han, W.-G.; Noodleman, L. *Inorg. Chem.* **2004**, *43*, 6858−6858.
(48) Sinnecker, S.; Slep, L. D.; Bill, E.; Neese, F. *Inorg. Chem.* **2005**, *44*, 2245−2254.
(49) Tissandier, M. D.; Cowen, K. A.; Feng, W. Y.; Gundlach, E.; Cohen, M. H.; Earhart, A. D.; Coe, J. V.; Tuttle, T. R. *J. Phys. Chem. A* **1998**, *102*, 7787−7794.
(50) Truhlar, D. G.; Cramer, C. J.; Lewis, A.; Bumpus, J. A. *J. Chem. Educ.* **2004**, *81*, 596−604.
(51) Truhlar, D. G.; Cramer, C. J.; Lewis, A.; Bumpus, J. A. *J. Chem. Educ.* **2007**, *84*, 934.
(52) Tawa, G. J.; Topol, I. A.; Burt, S. K.; Caldwell, R. A.; Rashin, A. A. *J. Chem. Phys.* **1998**, *109*, 4852−4863.
(53) Dyer, B. D. *A Field Guide to Bacteria*; Cornell University Press: Ithaca, NY, 2003.
(54) Kent, T. A.; Munck, E.; Dunham, W. R.; Filter, W. F.; Findling, K. L.; Yoshida, T.; Fee, J. A. *J. Biol. Chem.* **1982**, *257*, 12489−12492.
(55) Kent, T. A.; Young, L. J.; Palmer, G.; Fee, J. A.; Munck, E. *J. Biol. Chem.* **1983**, *258*, 8543−8546.
(56) Chang, H. Y.; Choi, S. K.; Vakkasoglu, A. S.; Chen, Y.; Hemp, J.; Fee, J. A.; Gennis, R. B. *Proc. Natl. Acad. Sci. U. S. A.* **2012**, *109*, 5259−5264.
(57) Sharma, V.; Karlin, K. D.; Wikstrom, M. *Proc. Natl. Acad. Sci. U. S. A.* **2013**, *110*, 16844−16849.
(58) Mayhew, S. G. *Eur. J. Biochem.* **1978**, *85*, 535−547.
(59) Gerscher, S.; Hildebrandt, P.; Buse, G.; Soulimane, T. *Biospectroscopy* **1999**, *5*, S53−S63.
(60) Dougherty, D. A. *Science* **1996**, *271*, 163−168.

DOI: 10.1021/acs.inorgchem.5b00700
Inorg. Chem. 2015, 54, 7272−7290